Glycogen phase separation drives macromolecular rearrangement and asymmetric division in *E. coli*

Yashna Thappeta[1,2,†], Silvia J. Cañas-Duarte[1,4,†], Till Kallem[5], Alessio Fragasso[1,2], Yingjie Xiang[6], William Gray[6], Cheyenne Lee[6††], Lynette Cegelski[5], Christine Jacobs-Wagner[1,2,3,4*]

[†]These authors contributed equally to this work

[1]Sarafan Chemistry, Engineering, and Medicine for Human Health Institute, Stanford University, Stanford, CA, USA

[2]Department of Biology, Stanford University, Stanford, CA, USA

[3]Department of Microbiology and Immunology, Stanford University, Stanford, CA, USA

[4]Howard Hughes Medical Institute, Stanford University, Stanford, USA

[5]Department of Chemistry, Stanford University, Stanford, CA, USA

[6]Mechanical Engineering and Materials Science, Yale University, New Haven, CT

[*]For correspondence: jacobs-wagner@stanford.edu

Present address:

[††]Department of Microbiology and Immunology, Emory University, Atlanta, GA

ABSTRACT

Bacteria often experience nutrient limitation in nature and the laboratory. While exponential and stationary growth phases are well characterized in the model bacterium *Escherichia coli*, little is known about what transpires inside individual cells during the transition between these two phases. Through quantitative cell imaging, we found that the position of nucleoids and cell division sites becomes increasingly asymmetric during transition phase. These asymmetries were coupled with spatial reorganization of proteins, ribosomes, and RNAs to nucleoid-centric localizations. Results from live-cell imaging experiments, complemented with genetic and ^{13}C whole-cell nuclear magnetic resonance spectroscopy studies, show that preferential accumulation of the storage polymer glycogen at the old cell pole leads to the observed rearrangements and asymmetric divisions. In vitro experiments suggest that these phenotypes are likely due to the propensity of glycogen to phase separate in crowded environments, as glycogen condensates exclude fluorescent proteins under physiological crowding conditions. Glycogen-associated differences in cell sizes between strains and future daughter cells suggest that glycogen phase separation allows cells to store large glucose reserves without counting them as cytoplasmic space.

KEYWORDS

Asymmetric division/ bacteria/ glycogen/ nutrient limitation/ phase separation

INTRODUCTION

Spatial order is an inherent feature of living cells across the tree of life. In eukaryotic cells, this is best exemplified by the presence of membrane-bound organelles. These cells also display extensive membrane-less organization, including those mediated by liquid-liquid phase separation (LLPS) between various cellular components (Alberti & Hyman, 2021; Banani *et al*, 2017; Boeynaems *et al*, 2018; Hyman *et al*, 2014; Rostam *et al*, 2023). While bacteria generally lack membrane-bound organelles, they also exhibit spatial organization at multiple levels (Surovtsev & Jacobs-Wagner, 2018), in the form of protein localization, chromosome structure, and LLPS involving proteins and/or nucleic acids, to name a few (Azaldegui *et al*, 2021; Bakshi *et al*, 2012; Cohan & Pappu, 2020; Landgraf *et al*, 2012). Reliance on subcellular organization is particularly evident in bacteria that undergo developmental programs and/or have dimorphic life cycles (e.g., sporulating bacteria, asymmetrically dividing α-proteobacteria). However, even bacteria with comparatively simpler life cycles such as *E. coli* display intracellular organization. For example, *E. coli* divides precisely in the middle of the cell. This spatial regulation is mediated by two separate mechanisms. The time-average pole-to-pole oscillation of Min proteins positions the FtsZ cytokinetic ring at mid-cell (Lutkenhaus, 2008; Shih & Zheng, 2013), while nucleoid occlusion prevents cell constriction from occurring over nucleoid regions (Woldringh *et al*, 1990). Furthermore, *E. coli* spatially organizes two of its most important macromolecules: the chromosome and polysomes (mRNAs in complex with ribosomes engaged in translation). The chromosome, which compacts into a meshwork structure known as the nucleoid, is spatially positioned inside cells, either near the cell center prior to DNA replication or near the ¼ and ¾ cell positions after DNA replication

62 and segregation (Badrinarayanan *et al*, 2012; Bates & Kleckner, 2005; Sherratt, 2003).
63 Polysomes adopt a near-opposite localization profile. They are depleted in the nucleoid
64 and enriched in nucleoid-free regions, including at the cell poles and between segregated
65 nucleoids (Azam *et al*, 2000; Bakshi *et al*, 2012; Chai *et al*, 2014). This anticorrelated
66 pattern is thought to be mediated by steric exclusion of these two macromolecules. In
67 contrast, smaller components such as free ribosomal subunits and cytoplasmic proteins
68 can diffuse throughout the nucleoid unimpeded (Amselem *et al*, 2023; Bakshi *et al*, 2012;
69 Sanamrad *et al*, 2014), resulting in homogeneous distribution throughout the cytoplasm.
70 This archetypical macromolecular organization is reproduced every generation.

71 The bulk of our knowledge of *E. coli* (and other well-studied bacteria) has largely
72 been derived from exponentially growing cultures. In their natural environments, *E. coli*
73 and other bacteria often experience nutrient deprivation to which they must adapt
74 (Dworkin & Harwood, 2022). In the laboratory, this deprivation is reproduced in batch
75 cultures when cells exit exponential growth and transition to stationary phase due to the
76 consumption of the available nutrients. Growth arrest is, however, not immediate. As
77 nutrient availability decreases, cell growth slows progressively until the cell density
78 reaches saturation marking the onset of stationary phase (Dworkin & Harwood, 2022).
79 During this transition, cells are thought to block new rounds of DNA replication before
80 they stop dividing, ultimately entering stationary phase with a smaller size and lower
81 chromosome content on average relative to their exponential phase counterparts
82 (Åkerlund *et al*, 1995). Yet, the transition between exponential growth and stationary
83 phase remains under-characterized, especially at the single-cell and subcellular
84 organizational levels. This study sets out to fill this gap in knowledge.

85 **RESULTS**

86

87 **Population characteristics change along the culture growth curve.**

88 We first used microscopy and DNA staining to quantify various cellular characteristics
89 (cell area, nucleoid positioning, cell constriction degree and position, etc.) along the
90 growth curve of liquid cultures of *E. coli* at 30˚C in M9 medium containing 0.2% glucose,
91 casamino acids and thiamine (M9GluCAAT). Under our experimental conditions, cultures
92 exhibited exponential growth up to an optical density (OD) at 600 nm of about 1.0, after
93 which population growth slowed down gradually until reaching saturating ODs around 3.0
94 (Fig 1A). While the culture might experience a diauxic shift in this medium when
95 transitioning between exponential and stationary phases, we will hereafter refer to this
96 period of sub-exponential growth (between ODs ~1 and ~3) as "transition phase" for
97 simplicity (Fig 1A). Imaging live cells from the same liquid culture at a high sampling
98 resolution along the growth curve was technically impractical with our set-up. Therefore,
99 we imaged cells from independent cultures at various ODs on different days and
100 examined how cellular characteristics may change as a function of the OD.

101 As expected, (Buchanan, 1918; Morita, 1990; Bakshi *et al*, 2021), we found that
102 the average cell area decreased with increasing ODs (Fig 1B). The number of nucleoids
103 per cell also decreased as cells entered transition phase (Fig 1C). As a result, the fraction
104 of cells with a single nucleoid increased in transition phase, reaching a plateau at OD ~
105 1.5 (Fig 1D) before the cell density became saturated. Meanwhile, the fraction of cells
106 undergoing constriction at the division site gradually decreased around the onset of
107 transition phase (OD ~1) and continued to decrease until the culture reached stationary

108 phase (Fig 1E). These results are consistent with cells undergoing one or more so-called
109 “reductive divisions” after DNA replication initiation has stopped (Nyström, 2004; Nyström
110 & Kjelleberg, 1989). This uncoupling between DNA replication and cell division explains
111 the reduction in chromosome copy number per cell by the time the culture enters
112 stationary phase (Åkerlund *et al*, 1995).

113 To our surprise, while the position of the cell constriction site was symmetric across
114 cell populations sampled during exponential phase (OD < 1), it became increasingly
115 asymmetric during sub-exponential growth in the transition phase (OD > 1) (Fig 1F, Fig
116 EV1). This was accompanied by an increase in asymmetric nucleoid positioning (Fig 1G,
117 Fig EV1), which may contribute to the previously reported increase in nucleoid position
118 variability in stationary phase (Chai *et al*, 2014).

119

120 **Cells exhibit asymmetric distributions of ribosomes, RNAs, and cytosolic protein**
121 **probes in transition phase.**

122 Given the marked offset in division site and nucleoid positioning during transition phase,
123 we wondered whether the intracellular organization of other macromolecules also
124 changes when cells exit exponential phase. First, we considered ribosomes and
125 cytoplasmic proteins by examining the localization of RplA-mCherry and freely diffusing
126 msfGFP, respectively. As expected, in exponential phase, msfGFP was distributed
127 homogeneously throughout the cytoplasm while the RplA-mCherry signal was enriched
128 outside the DAPI-stained nucleoid regions (Fig 2A). The latter was consistent with most
129 ribosomes forming polysomes (Phillips *et al*, 1969; Mohapatra & Weisshaar, 2018) and
130 polysomes being partially excluded from the nucleoid. In contrast, in transition phase,

131 both msfGFP and RplA-mCherry signals were depleted from the nucleoid-distal cell poles
132 while being enriched within and around the offset nucleoid (Fig 2A). This change in
133 localization pattern was confirmed quantitatively across the cell population using the
134 signal correlation factor (SCF), which measures the correlation between two signals
135 within each cell at the pixel resolution (Gray *et al*, 2019). In exponential phase, the SCF
136 between the DAPI (nucleoid) and RplA-mCherry (ribosome) signals was largely negative
137 across cells, indicating a predominant anti-correlation. The SCF switched to positive
138 values in transition phase (Fig 2B). The SCF values between DAPI and msfGFP also
139 became more positive (Fig 2C), reflecting the increased colocalization between msfGFP
140 and the nucleoid in transition phase. We observed the same intracellular reorganization
141 in transition phase using other ribosomal protein fusions (RplA-msfGFP, RplA-mCherry,
142 or RpsB-msfGFP) and a genetically unrelated cytoplasmic protein probe (mScarlet) (Fig
143 EV2A-B).

144 Furthermore, GFP derivatives with surface net charges varying between -30 and
145 +15, which reflects most of the range of net surface charges in the *E. coli* proteome
146 (Schavemaker *et al*, 2017), were similarly enriched in the nucleoid region during transition
147 phase (Fig EV2C). This shared localization phenotype across cytosolic protein probes of
148 different genetic origins and charges suggests that this subcellular reorganization is likely
149 common among proteins during transition phase.

150 To determine whether this change in localization pattern extends beyond
151 ribosomes and cytoplasmic protein probes, we also assessed RNA localization in two
152 ways. First, we used a cytosolic mutant variant of RNase E, RNase E ΔMTS, fused to
153 mCherry (Strahl *et al*, 2015), with the assumption that its localization will, at least in part,

154 reflect that of its RNA substrate. RNase E, which is involved in the degradation of mRNAs
155 and the processing of rRNAs (Strahl *et al*, 2015), is normally membrane-associated via a
156 short membrane-targeting sequence (MTS) (Khemici *et al*, 2008) and forms foci in the
157 presence of RNA (Strahl *et al*, 2015). In RNase E mutants lacking this sequence, the
158 protein is released into the cytoplasm (Khemici *et al*, 2008). We found that in exponentially
159 growing cells, the ΔMTS-mCherry variant of RNase E exhibited various degree of
160 accumulation in nucleoid-free regions (Fig 2D). This localization pattern changed during
161 transition phase, with RNase E ΔMTS-mCherry primarily colocalizing with the nucleoid
162 (Fig 2D). This switch was confirmed at the population level as the SCF values between
163 the DAPI and RNaseE ΔMTS-mCherry signals changed from negative to highly positive
164 values (Fig 2E), indicative of signal colocalization in transition phase.
165 In addition, we imaged cells incubated with SYTO RNASelect, a membrane-
166 permeable fluorogenic RNA dye that has been validated in *E. coli* (Bakshi *et al*, 2014).
167 We found that the RNASelect signal, which was relatively homogeneously distributed in
168 exponential phase cells, relocated to the nucleoid region during transition phase (Fig
169 EV2D). This shift was reflected by the increase in SCF values between the DAPI and
170 RNASelect signals (Fig EV2E). Taken together, our results show that all major
171 cytoplasmic macromolecules undergo significant localization changes inside cells as they
172 exit exponential growth.
173
174
175

176 **Reorganization of macromolecules cannot be explained by membrane retraction or**
177 **nucleoid association.**
178 It was recently reported that, in stationary phase or upon acute starvation, the inner
179 membrane of *E. coli* cells can retract–predominantly at the new pole–due to sudden loss
180 of cytoplasmic water and atrophy of the cytoplasmic volume (Shi *et al*, 2021). Therefore,
181 we wondered whether a membrane collapse could explain both the observed nucleoid
182 position asymmetry and enrichment of cytoplasmic components in the nucleoid space in
183 transition phase. Based on phase contrast images and cell staining with MitoTracker
184 Green, a fluorescent dye that labels the inner membrane (Shi *et al*, 2021), we found no
185 evidence of membrane retraction during transition phase (Fig 3A). Furthermore,
186 timelapse microscopy on agarose pads revealed that the nucleoids of cells in transition
187 phase remained closer to the new pole (Fig 3B, Video EV1). The ribosome signal largely
188 followed the nucleoid, resulting in ribosome depletion specifically at the old pole (Fig 3B,
189 Video EV1), the opposite pole reported to typically undergo membrane retraction (Shi *et*
190 *al*, 2021).
191 To test whether the depletion of ribosomes and protein probes was associated with
192 the old pole or any DNA-free regions, we treated the cells with cephalexin. This antibiotic
193 irreversibly inhibits the cell division protein FtsI (Hedge & Spratt, 1985; Pogliano *et al*,
194 1997) without affecting cell growth (Rolinson, 1980) to generate filamentous cells with
195 multiple nucleoids. We found that, in transition phase, ribosomes and protein probes
196 colocalize with the nucleoids and are depleted in nucleoid-free spaces, including between
197 nucleoids (Fig 3C). We confirmed these findings using a FtsZ-depletion strain as an
198 orthogonal method to generate filamentous polynucleoid cells (Fig EV3).

199 Given the colocalization with the nucleoid, we questioned whether the observed
200 rearrangement of cytoplasmic components may be driven by a (direct or indirect)
201 association with the nucleoid. Two lines of evidence suggested otherwise. First, in
202 filamentous cephalexin-treated cells, we occasionally observed a sharp accumulation of
203 fluorescently labeled ribosomes and msfGFP in nucleoid-free space (Fig 3D, bracket area
204 and purple arrowhead). Second, we noted that the intensity profiles of the msfGFP signal
205 extends beyond that of the DNA signal (Fig 2A). This was not due to the lower excitation
206 wavelength of DAPI relative to that of the fluorescent protein probes, as the msfGFP
207 signal also extended beyond the nucleoid signal when labeled with DNA-binding protein
208 HupA fused to mCherry (Fig 3E), which emits at a higher wavelength than msfGFP.
209 Together, this suggests that a cytosolic element that accumulates in nucleoid-free space
210 likely excludes ribosomes, proteins and possibly RNAs during transition phase.
211
212 **Glycogen accumulation contributes to the asymmetric localization pattern of the**
213 **nucleoid, ribosomes, and proteins.**
214 In our search for the cytosolic element driving the observed intracellular reorganization,
215 we used whole-cell ^{13}C cross-polarization magic-angle spinning (CPMAS) solid-state
216 NMR to evaluate whether the carbon composition of cells changes between exponential
217 and transition phases. We found that in comparison to exponential-phase samples,
218 transition-phase samples showed a large increase in carbon intensities in the ^{13}C CPMAS
219 NMR spectra between 110 and 55 ppm (Fig 4A), characteristic of polysaccharide
220 contributions. We speculated that these carbon intensity increases might correspond to
221 an accumulation of glycogen, a glucose polymer that *E. coli* cells can accumulate under

222 nutrient limitation (Preiss, 1984; Wang *et al*, 2019a; Wilson *et al*, 2010; Bourassa &
223 Camilli, 2009; Jones *et al*, 2008; Preiss & Romeo, 1994), preferentially at the old pole
224 (Boehm *et al*, 2016). Indeed, the ^{13}C CPMAS NMR spectra of bovine and mussel-derived
225 glycogen were consistent with the spectral changes observed in transition-phase samples
226 (Fig 4A). To test this possibility, we generated a glycogen-deficient strain (Δ*glgBXCAP*)
227 by deleting the glycogen metabolic operon. The ^{13}C CPMAS NMR spectrum of transition-
228 phase samples from this glycogen-deficient strain lacked the large carbon intensity
229 increases observed in the wild-type (WT) strain that we attribute to glycogen (Fig 4A).

230 To visualize glycogen in live cells and compare its localization with that of protein
231 probes, we built a glycogen biosensor and placed its synthesis under the control of an
232 isopropyl β-D-1-thiogalactopyranoside (IPTG)-inducible promoter. Inspired by a previous
233 eukaryotic study (Skurat *et al*, 2017), we generated a translational mGFPmut3 fusion to
234 the N-terminus of the starch binding domain (CBM20) of the human protein Stbd1.
235 mGFPmut3 was chosen for this fusion due to its monomeric characteristics and low
236 probability of forming aggregates (Landgraf *et al*, 2012). We found that the basal (leaky)
237 expression from a chromosomally inserted P_{tac} promoter was sufficient to visualize the
238 glycogen sensor in transition phase cells. In WT cells, the sensor accumulated in the
239 nucleoid-free space, which was depleted of the free mScarlet fluorescent protein (Fig 4B).
240 This negative correlation between the biosensor and the scarlet signal localization, which
241 was demonstrated at the population level by strong negative SCF values (Fig 4C), is
242 consistent with glycogen excluding freely diffusing proteins. Indeed, diffuse distribution of
243 mScarlet was restored in Δ*glgBXCAP* cells during transition phase (Fig 4B).

244 In WT cells, glycogen and the nucleoid appeared to exclude each other, as
245 suggested by the strong negative SCF values between DAPI and the glycogen sensor
246 signal (Fig 4C). As such, we predicted that glycogen accumulation at the old pole is, at
247 least in part, responsible for the asymmetric position of the nucleoid toward the new pole
248 in transition phase. To measure the asymmetry of glycogen accumulation, we calculated
249 the difference in the area of glycogen (biosensor) signal between the two poles, where
250 larger deviations from zero indicate a larger asymmetry in glycogen accumulation. We
251 found a positive correlation between glycogen accumulation asymmetry and nucleoid
252 position asymmetry (Fig 4D). That is, cells with a larger asymmetry in glycogen sensor
253 signal between the poles tended to exhibit a greater offset in nucleoid position, consistent
254 with our prediction.

255 Another line of support for glycogen driving the transition-phase phenotypes was
256 provided by observations of cephalexin-treated cells expressing the glycogen sensor and
257 fluorescently labeled ribosomes. Whenever we observed a band of ribosome enrichment
258 in nucleoid-free space (as first illustrated in Fig 3D), this region was flanked by glycogen
259 accumulations (Fig 4E). This observation was independently corroborated using the
260 glucose analog 2-NBDG (2-(N-(7-nitrobenz-2-oxa-1,3-diazol-4-yl)amino)-2-
261 deoxyglucose) (Yoshioka *et al*, 1996b). This glucose analog is readily taken up by *E. coli*
262 (Yoshioka *et al*, 1996b, 1996a) where it can be incorporated into the glycogen polymer
263 (Zhu *et al*, 2020). However, upon uptake, the analog is modified to a non-fluorescent form
264 resulting in fluorescence signal loss (Yoshioka *et al*, 1996a), leading to a low signal-to-
265 noise ratio. Nevertheless, the signal intensity was sufficient to reveal 2-NBDG

266 accumulations flanking ribosome enrichment in nucleoid-free space of cephalexin-treated
267 cells producing glycogen during transition phase (Fig EV4).
268
269 **Glycogen condensates exclude fluorescent proteins in vitro.**
270 In the bacteriology literature, glycogen accumulations are often described as “granules”
271 or “inclusion bodies” due to their round or oval shapes when visualized by electron
272 microscopy (Shively, 1974; Preiss, 1984; Liu *et al*, 2021b; Alonso-Casajús *et al*, 2006;
273 Preiss & Romeo, 1994). These terms can give the impression of a solid. However, recent
274 work in liver cells has reported that glycogen can undergo LLPS in the cytosol (Liu *et al*,
275 2021a). Glycogen extracted from mouse livers has also been shown to undergo LLPS in
276 vitro, in a concentration-dependent manner, in the presence of a crowding agent (Liu *et*
277 *al*, 2021a). Considering this study, we asked the following questions: does glycogen form
278 liquid condensates under in vitro conditions that mimic the *E. coli* cytoplasm and, if so,
279 can glycogen condensates exclude proteins?
280 For our in vitro conditions, we focused on three aspects of the *E. coli* cytoplasm:
281 glycogen concentration, ionic strength, and crowding. Given that glycogen represents
282 0.75-1.2% of the cell’s wet weight in stationary phase after growth in Luria Broth (Wang
283 *et al*, 2019a; Neidhardt & Curtiss, 1996), we assumed the glycogen concentration range
284 to be between 8 and 13 g/L based on a cell density of 1.1 g/mL (Baldwin *et al*, 1995) (see
285 Table 1). We elected to use glycogen from mussels because of its commercial availability
286 at a high (>99%) purity. We used a potassium phosphate buffer (pH = 7.0) that includes
287 85 mM NaCl, 250 mM KCl, 2.5 mM $MgCl_2$ and 0.1 mM $CaCl_2$ to reflect the ionic strength
288 of the *E. coli* cytoplasm (Schultz *et al*, 1962; Alatossava *et al*, 1985; Gangola & Rosen,

289 1987; Szatmári *et al*, 2020). Hereafter, we refer to this solution as the "intracellular salt
290 (IS) buffer". As a stand-in for cytoplasmic macromolecules, we used the synthetic
291 biocompatible nonionic polymer polyethylene glycol (abbreviated to PEG or PEO
292 depending on its molecular weight). PEG/PEO polymers are available in a broad range
293 of molecular weights. Since size, not molecular weight, is the relevant variable for a
294 crowder (Asakura & Oosawa, 1954, 1958; Sharp, 2015), we used dynamic light
295 scattering to measure the hydrodynamic (Stokes) diameter of PEG and PEO polymers of
296 different molecular weights in the IS buffer (Fig 5A). Our results agree well with an
297 empirical relationship determined in deionized water (pH = 5.5) (Devanand & Selser,
298 1991) (Fig 5A, line), despite the differences in pH and ionic concentrations of the solvents
299 used.

300 We first chose 3 kDa PEG (~3 nm of diameter) to mimic proteins, which are the
301 most abundant macromolecular crowders in the *E. coli* cytoplasm (Neidhardt & Curtiss,
302 1996) with diameters ranging between 2 and 6 nm (Erickson, 2009; Hink *et al*, 2000;
303 Lukatsky & Shakhnovich, 2008). We found that glycogen (10 g/L), which was visualized
304 using ConA-FITC labeling (Lvov *et al*, 1996; Becker *et al*, 1976), transitioned from
305 homogeneously mixed in the solution to forming droplets as the concentration of 3 kDa
306 PEG increased from 9 to 20 mM (Fig 5B). Consistent with the liver study (Liu *et al*, 2021a),
307 these droplets exhibited liquid-like behaviors, demonstrating fusion events on the minute
308 time scale (Fig 5C, Video EV2). These fusion events resulted in coalescence of small
309 condensates into larger ones at longer time scales (e.g., 30 min, Fig 5D), which is
310 consistent with LLPS. At higher 3 kDa PEG concentrations, glycogen underwent a second
311 phase transition, in which the droplets collapsed into amorphous aggregates (Fig 5B).

312 Timelapse imaging of these aggregates showed no evidence of fusion upon collision
313 (e.g., Video EV3), consistent with a solid-like form.

314 In addition, we confirmed that LLPS of glycogen is dependent on its own
315 concentration. As shown in a phase diagram (Fig 5E), higher concentrations of glycogen
316 required less crowder to form liquid condensates. By using PEG/PEO of higher molecular
317 weights, we also demonstrated that the formation of glycogen droplets was very sensitive
318 to the size of the crowder (Fig 5F). For instance, at least 19 mM of 3 kDa PEG was
319 required for LLPS to occur while the same could be achieved with only 150 μM of 100
320 kDa PEO or 10 μM of 1 MDa PEO. The two larger crowders (100 kDa and 1 MDa) were
321 selected because their diameters (at concentrations below their overlap concentrations),
322 estimated to be ~30 nm and ~70 nm (Fig 5A), are the closest to the size of ribosomes in
323 free and polysome forms, respectively (Brandt *et al*, 2009; Nilsson *et al*, 1997).

324 As both proteins and ribosomes (largely assembled into polysomes) are excluded
325 from glycogen in vivo (Fig 2A), we hypothesized that the combined effect of their cellular
326 concentrations could lead to LLPS of glycogen. Consistent with this hypothesis,
327 combining the stand-in crowders (10 mM of 3 kDa PEG, 25 μM of 100 kDa PEO, and 5
328 μM of 1 MDa PEO) at biologically relevant concentrations for proteins, ribosomes and
329 polysomes (see Tables 1 and 2) resulted in the formation of glycogen droplets, while no
330 crowder alone induced LLPS at these concentrations (Fig 5G). Note that, for the 1 MDa
331 PEO crowder, the concentrations required to drive LLPS are above its “overlap”
332 concentration (self-crowding) (see Materials and Methods) and thus our estimated
333 diameter for this crowder shown in Fig 5A is likely overestimated. Regardless of the

334 crowder size used, glycogen LLPS was found to be reversible, as diluting the crowder
335 after the droplets formed led to their immediate (< 1 min) disappearance (Fig 5H).
336 To test if glycogen LLPS could explain the exclusion of proteins observed in vivo,
337 we added GFP to the in vitro reactions and analyzed the spatial distribution of
338 fluorescence intensity in relationship with the phase contrast signal from the glycogen
339 droplets. We found that glycogen condensates partially excluded fluorescent proteins (Fig
340 5I). This was also observed by performing z-stack imaging of the glycogen condensates
341 suspended in the liquid column, in which exclusion remains observable despite the added
342 background from the contribution of GFP molecules in surrounding focal planes (Video
343 EV4). This protein exclusion was observed in all tested combinations of PEG/PEO
344 crowder sizes (2.7–74 nm) and concentrations that led to glycogen condensate formation
345 (Table 3).
346 Our in vitro data, together with estimates of macromolecule concentration inside
347 cells (Tables 1-2) and the shape of so-called glycogen "granules" in electron micrographs
348 (Preiss, 1984; Alonso-Casajús *et al*, 2006), are more consistent with glycogen forming
349 liquid condensates over solid condensates inside cells (see also Discussion). However,
350 technical limitations prevent us from testing whether glycogen condensates in *E. coli* cells
351 are truly liquid or more gel-like (see Discussion). Therefore, we will simply refer to the
352 localized glycogen accumulations as "condensates" hereafter. Importantly, our in vitro
353 findings argue that phase separation of glycogen into a liquid droplet alone can explain
354 the exclusion of proteins from glycogen-rich regions in transition phase cells.
355
356

357 **Glycogen condensates are associated with an increase in cell size.**

358 The preferential accumulation of these condensates at the old pole results in partial
359 exclusion of cytoplasmic components from this location. If division was symmetric and
360 produced two daughter cells of equal size, the daughter cell that inherits the glycogen-
361 rich cell pole would receive less cytoplasmic content than its sibling. However, analysis
362 of constricting cells in transition phase revealed that the future daughter cells with more
363 glycogen tended to be bigger than their future siblings with less glycogen because of
364 asymmetric cell division ($\rho = 0.54$, Fig 6A-B). While there was considerable noise in our
365 measurements, a linear fit across the data suggested a near direct proportionality (i.e.,
366 slope ~ 1) between the difference in glycogen amount and the difference in cell size
367 between future daughter cells (Fig 6B). Thus, cells do not appear to "count" glycogen
368 condensates as cytoplasmic space and effectively create extra (i.e., bonus) space to
369 accommodate the large amount of glycogen produced in transition phase.

370 This bonus-space hypothesis predicts that glycogen-deficient cells should, on
371 average, be smaller than cells producing glycogen condensates. Since cell size changes
372 with the OD during transition phase (Fig 1B), we performed co-cultures of Δ*glgBXCAP*
373 and parent strains to examine their cell size at precisely the same OD. We used the
374 expression of different fluorescent proteins to distinguish between the glycogen-
375 producing and glycogen-deficient genetic backgrounds (Fig 6C). Consistent with our
376 hypothesis, co-cultures of mVenus-expressing Δ*glgBXCAP* and mSCFP3-expressing WT
377 cells revealed that glycogen-deficient cells were, on average, about ~13% smaller than
378 glycogen-producing cells in transition phase (mix 1, Fig 6D). We obtained similar results
379 when the fluorophores were swapped between the WT and Δ*glgBXCAP* backgrounds

380 (mix 2, Fig 6D), indicating that the cell size difference was independent of the type of
381 fluorescent protein used to identify cells. This cell size difference is unlikely to be due
382 solely to a growth benefit associated with glycogen metabolism since it is generated in
383 the mother cell before cell constriction is complete, i.e., when the cytoplasm (and thus,
384 the metabolism) of the two future daughter cells is still shared (Fig 6A-B).

385 We reasoned that glycogen condensates effectively "push" the nucleoid away from
386 the old pole through mutual exclusion, which, in turn, offsets the division site toward the
387 new pole. Consistent with this idea, the extent of asymmetry in nucleoid and division
388 positions in transition phase was considerably reduced in Δ*glgBXCAP* cells relative to the
389 WT (Fig 6E, Fig EV5A). We concluded that the propensity of glycogen to transition into
390 condensates in the presence of crowders promotes asymmetric division in *E. coli*.

391

392 **DISCUSSION**

393 Our quantitative analysis of transition phase at the subcellular and single-cell level reveals
394 a picture of *E. coli* cell biology that departs from the textbook view in several ways.

395 The first difference relates to division. Asymmetric divisions are typically thought
396 of as exceptions in the bacterial world, restricted to a small subset of bacteria that undergo
397 developmental programs that produce either two functionally divergent daughter cells at
398 each cell cycle (e.g., *Caulobacter crescentus*) or an endospore in response to starvation
399 (e.g., *Bacillus subtilis*). In fact, *E. coli* is often used as the quintessential example of a
400 symmetrically dividing bacterium. However, its division has primarily been examined
401 during exponential growth. Our study shows that asymmetric division and production of
402 daughter cells of unequal sizes become common in *E. coli* when the population deviates

403 from exponential phase (Fig 1F), likely contributing to the documented increase in cell
404 size variability in stationary phase (Bakshi *et al*, 2021).

405 We propose that these asymmetric divisions occur because of the propensity of
406 glycogen to spontaneously phase separate into condensates in crowded environments
407 (Fig 5) (Liu *et al*, 2021a). Our data suggest that these condensates preferentially
408 accumulate at the old cell pole through inheritance from the previous generation,
409 effectively "pushing" the nucleoids closer to the new pole (Fig 3B). In fact, such nucleoid
410 pushing can be artificially exacerbated in exponential phase through mutation of the
411 carbon storage regulator gene *csrA*, which results in massive glycogen overproduction
412 (Boehm *et al*, 2016). We propose that the nucleoid offset generated by glycogen
413 condensates promotes off-center division through nucleoid occlusion, a fail-safe
414 mechanism that prevents cell constriction over nucleoid regions to prevent chromosome
415 scissoring events (Woldringh *et al*, 1990). Large polar glycogen condensates may also
416 interfere with the oscillatory behavior of the Min system, which determines the position of
417 the FtsZ cytokinetic ring (Shih & Zheng, 2013; Lutkenhaus, 2008).

418 Cells in transition phase also diverge from the traditional view with respect to their
419 spatial organization of macromolecules such as ribosomes/polysomes, proteins, and
420 RNAs. In transition phase, these macromolecules adopt a more chromosome-biased
421 distribution (Fig 2), which is largely caused by glycogen exclusion. Our in vitro
422 experiments suggest that glycogen does not have to assemble into a solid (i.e., a granule
423 or an inclusion body) to exclude protein probes, as liquid condensates could achieve
424 similar results (Fig 5I). In fact, based on our calculations (Tables 1-2) and in vitro
425 experiments (Fig 5E-G), the physiological range of intracellular concentrations of proteins,

426 ribosomes, and polysomes is compatible with the combined PEG/PEO concentrations
427 needed for glycogen to phase separate into liquid condensates, but not to collapse into a
428 solid state. Collapsing glycogen into aggregates requires crowder concentrations that well
429 exceed the macromolecular concentration expected inside cells (Fig 5E, Tables 1-2).
430 Furthermore, unlike the amorphous glycogen aggregates, the liquid condensates
431 obtained in vitro are morphologically consistent with the round and oval shapes of
432 glycogen bodies observed in electron micrographs of starved cells (Alonso-Casajús *et al*,
433 2006). Consistent with our results, a recent preprinted study has shown that concentrating
434 macromolecules in frog egg extracts by ≥ 1.4-fold demixes the cytoplasm into two liquid
435 phases: a glycogen-enriched phase and a ribosome-enriched phase (Pelletier *et al*,
436 2021). In *E. coli,* and presumably other glycogen-producing bacteria, this cytoplasmic
437 demixing may be even more likely, as the bacterial cytoplasm is thought to be more
438 crowded than the eukaryotic cytosol based on fluorescent protein diffusion measurements
439 (Elowitz *et al*, 1999; Swaminathan *et al*, 1997; Potma *et al*, 2001; Konopka *et al*, 2009).
440 It remains possible that glycogen condensates inside *E. coli* cells are not perfectly
441 liquid and may be more gel-like. The small size of bacterial cells and glycogen
442 condensates make it impractical to test for liquid-like behaviors like droplet fusions in vivo,
443 as it is often done in LLPS studies in eukaryotic cells (Alberti *et al*, 2018, 2019; Hoang *et*
444 *al*, 2023; Liu *et al*, 2021a). Assays based on fluorescence recovery after photobleaching
445 (FRAP), which can be implemented to probe the diffusivity of proteins when they form
446 condensates (Alberti *et al*, 2019; Wang *et al*, 2019b), are also prohibited by the weak
447 fluorescent signal of the glucose analog 2-NBDG once incorporated into glycogen (Fig
448 EV4). FRAP experiments with the glycogen biosensor are not appropriate either, as any

449 observed dynamics would reflect not only the motion of glycogen molecules within the
450 condensates, but also the binding kinetics of the biosensor to glycogen. While these
451 limitations persist, our evidence argues that glycogen accumulations inside cells are more
452 likely to be the product of phase separation into condensates (whether liquid or gel-like)
453 than the result of glycogen assembling into solid structures such as granules or inclusion
454 bodies.

455 Glycogen is well-known to provide a mean for cells to store a large amount of
456 glucose without dramatically increasing the osmolarity of their cytoplasm, as a branched
457 glycogen polymer contains thousands of glucose residues (Bezborodkina *et al*, 2018).
458 Whether its phase separation into condensates is associated with beneficial or
459 detrimental implications for the cell is an interesting question that warrants further
460 exploration. For instance, since glycogen has viscogenic properties (Persson *et al*, 2020),
461 compartmentalization into condensates might prevent high levels of glycogen from
462 increasing the cytoplasmic viscosity, which could decrease macromolecular diffusion to
463 deleterious levels. Furthermore, if glycogen did not phase separate (i.e., remained soluble
464 and homogeneously distributed in the cytoplasm), distribution of glucose reserves
465 between daughter cells would be near equal. In contrast, our data suggest that phase
466 separation leads to an asymmetric distribution that increases with each division through
467 additive glycogen accumulation at the old pole. This unequal distribution endows a
468 fraction of the cell population with larger energy reserves, which may increase the survival
469 probability of the species under prolonged periods of duress. Glycogen has indeed been
470 reported to facilitate the adaptation of environmental, phototrophic, and pathogenic
471 bacteria to starvation and other stresses (Sekar *et al*, 2020; Bourassa & Camilli, 2009;

472 Klotz *et al*, 2016; Klotz & Forchhammer, 2017; Gründel *et al*, 2012; Wang *et al*, 2020). As
473 for the partitioning of other macromolecules, their exclusion from glycogen condensates
474 does not appear to affect their distribution between daughter cells. This is because
475 division becomes asymmetric in the presence of glycogen condensates; the larger the
476 glycogen accumulation, the more asymmetric the division (Fig 6B), minimizing any
477 potential detrimental disparity in cytoplasm partitioning between daughter cells. In effect,
478 the cells appear to not "count" the space occupied by the glycogen condensates (Fig 6D-
479 E).

480 The relevance of our work may extend beyond *E. coli*, as glycogen metabolism is
481 widespread across bacteria (Almagro *et al*, 2015; Henrissat *et al*, 2002; Preiss & Romeo,
482 1990; Wang *et al*, 2019a; Wang & Wise, 2011). Induction of glycogen synthesis is a
483 common response when nutrients such as nitrogen, sulfur, or phosphate become limiting
484 (Holme *et al*, 1956, 1957; Madsen, 1963; Mulder *et al*, 1962; Sigal *et al*, 1964;
485 Zevenhuizen, 1966; Strange *et al*, 1961). Given that bacteria often live in nutrient-
486 fluctuating environments, our findings suggest that the cellular asymmetries in division
487 and macromolecule distribution may be more prevalent in the bacterial world than
488 currently appreciated. In addition, phase separation may be relevant to other bacterial
489 storage polymers besides glycogen. Polyphosphate, an energy-rich anionic polymer, is a
490 good candidate. It forms so-called granules in various bacteria (Albi & Serrano, 2016),
491 and timelapse experiments on starved *Pseudomonas aeruginosa* cells have shown that
492 these granules decrease in number while increasing in size during de novo biogenesis,
493 consistent with fusion events and liquid behavior (Racki *et al*, 2017). Future exploration

494 may shed light on the prevalence, role, and implications of phase separation across
495 storage polymers in different bacteria.
496
497 **METHODS**
498 **Bacterial strains and growth conditions**
499 Bacterial strains and descriptions of their constructions can be found in Tables 4 and 5.
500 P1 transductions were performed as previously described (Thomason *et al*, 2007) with
501 the exception that donor strains were grown without glucose supplementation. A lysate
502 of P1 phages was obtained from ATCC (25404-B1). Oligomers used for polymerase chain
503 reactions (PCR) are listed in Table 6. Lambda red recombination was performed as
504 previously described using the pKD46 (Datsenko & Wanner, 2000) or pSIM6 plasmids
505 (Diner *et al*, 2011). Unless otherwise indicated, cells were grown at 30°C in M9 medium
506 (26.11 mM Na_2HPO_4, 22 mM KH_2PO_4, 8.55 mM NaCl, 18.7 mM NH_4Cl, 2 mM $MgSO_4$ and
507 0.1 mM $CaCl_2$) supplemented with 0.2% glucose, 0.1% casamino acids and 1 µg/ml
508 thiamine (M9GluCAAT). Cells were first inoculated in the appropriate growth medium and
509 grown to stationary phase in culture tubes. They were then re-inoculated into fresh media
510 by diluting at least 10,000-fold and grown until they reached the indicated optical density
511 (OD) at 600 nm. When appropriate, ampicillin (100 µg/mL), kanamycin (50 µg/mL), or
512 chloramphenicol (30 µg/mL) was added to media for selection.
513 Strains expressing green fluorescent proteins with different net charges
514 (Schavemaker *et al*, 2017) were grown in M9GluCAAT and fluorescent protein
515 expression was induced with 0.4% arabinose upon re-inoculation of stationary phase

516 cultures. Given the richer medium condition from the addition of arabinose, the transition
517 phase OD ranged from 2.9 to 3.5 instead of 1.2 to 2.7.
518 FtsZ depletion experiments were conducted using strain CJW7588 in the presence
519 of 0.2% arabinose. For exponentially growing cultures, arabinose was added for the
520 equivalent of 2-3 doublings. For transition-phase cultures, arabinose was added in late
521 exponential phase (~OD 0.4-0.5) and imaged ~5 h later when cultures reached transition
522 phase ODs (the equivalent of 2-3 doublings) on an agarose pad made of spent medium.
523
524 **Dyes and labels**
525 To label the nucleoid, cells were incubated with 1 μg/ml 4′,6-diamidino-2-phenylindole
526 (DAPI) for 10 min prior to imaging. To visualize intracellular 2-NBDG localization, cells
527 were grown in M9CAAT supplemented with 0.2% L-arabinose to the desired OD and
528 incubated with 10 μM 2-NBDG for 10 min, then washed twice in prewarmed spent medium
529 filtered with a 0.22 μm filter. For the following dyes, concentrations were increased when
530 used on transition-phase cells as cell permeability seemed to decrease with increasing
531 ODs, consistent with a previous report (Bakshi *et al*, 2014). To visualize the inner
532 membrane of *E. coli* cells, MitoTracker Green (Shi *et al*, 2021) was added to the cell
533 culture at a final concentration of 100 nM (exponential phase) or 1 μM (transition phase)
534 and incubated for 30 min prior to imaging. To label RNA, SYTO RNASelect was used at
535 a final concentration of 500 nM (exponential phase) or 2.5 μM (transition phase) for 10
536 min and washed twice in filtered spent medium (Bakshi *et al*, 2014) prior to imaging.
537
538

539 **Cephalexin treatment**

540 For cephalexin treatment of exponentially growing cultures, the antibiotic (50 µg/mL) was
541 added for the equivalent of 2-3 doublings. For transition phase samples in M9GluCAAT,
542 cells were incubated with cephalexin (50 µg/mL) in late exponential phase (~OD 0.4-0.5)
543 and imaged ~5 h later when cultures reached transition phase (the equivalent of 2-3
544 doublings) on agarose pads made of spent medium containing cephalexin.

545

546 **Microscopy**

547 Unless otherwise indicated, cells were imaged on 1.5% agarose pads made with the
548 appropriate spent growth medium. For samples with high cell density in late transition or
549 stationary phase, cells were diluted in warm filtered spent medium prior to spotting on an
550 agarose pad for ease of cell segmentation.

551 Microscopy was performed using Nikon inverted microscope set-ups controlled by
552 the NIS-Elements AR software, with the following specifications. One of the set-ups
553 consisted of a Nikon Ti2-E inverted microscope equipped with a Perfect Focus System
554 (PFS), a motorized stage, a 100x Plan Apo 1.45NA Ph3 oil objective, a Photometrics
555 Prime BSI back-illuminated sCMOS camera, a Lumencor Spectra III LED light engine
556 excitation source, a polychroic mirror (FF-409/493/596-Di02 for by Shemrock) combined
557 with a triple-pass emitter (FF-1-432/523/702-25 by Shemrock) for GFP/DAPI/mCherry,
558 and a polychroic mirror (FF-459/526/596-Di01 by Shemrock) combined with a triple-pass
559 emitter (FF01-475/543/702-25 by Shemrock) for CFP/YFP/mCherry. Temperature was
560 set and maintained at the indicated value using a temperature chamber (Okolabs). The
561 second microscope set-up consisted of a Nikon Eclipse Ti microscope equipped with a

562 Hamamatsu ORCA-Flash 4.0 camera, a 100X objective (Nikon, OFN Ph3 DM, N.A. 1.45)
563 and a Spectra X light engine (Lumencor). The following Chroma filter sets were used to
564 acquire fluorescence images: DAPI (excitation ET350/50x, dichroic T400lp, emission
565 ET460/50 m), GFP (excitation ET470/40x, dichroic T425lpxr, emission ET525/50 m) and
566 mCherry/TexasRed (excitation ET560/40x, dichroic T585lpxr, emission ET630/75 m).
567 Temperature was maintained at 30°C using a customized enclosure and temperature
568 controller (Air-Therm SWT, World Precision Instrument) for timelapse imaging.
569 Temperature was also maintained for snapshots but did not affect transition-phase
570 phenotypes in the time window required for imaging (under 12 min).
571
572 **Image processing and analysis**
573 For cells imaged on agarose pads, cells were detected from phase contrast images using
574 the open-source software package Oufti (Paintdakhi *et al*, 2016). Cell contours were
575 curated using a trained support vector machine model to automatically remove poor and
576 incorrect cell detections (Gray *et al*, 2019). Nucleoid outlines were detected using the
577 objectDetection module of Oufti with the following detection parameters: manual
578 background threshold = 0.1; background subtraction method = 3; background subtraction
579 threshold = 0.1; background filter size = 8; smoothing range (pixels) = 3; magnitude of
580 LOG filter = 0.1; sigma of PSF = 1.62; fraction of object in cell = 0.40; and minimum object
581 area = 50. Parameters for cell and nucleoid detection were maintained across all cells
582 analyzed. Cell morphological features including cell length, cell area, number of nucleoid
583 objects, and cell constriction position were extracted from Oufti output using code
584 cellSizeCycle2 adapted from Govers et al (Govers *et al*, 2024). The cell constriction

585 positions have values between 0 and 1, with 0.5 corresponding to the cell center. The
586 absolute deviation from 0.5 was taken to reflect the absolute distance of division position
587 to cell center normalized by cell length. Degree of cell constriction was generated using
588 function constDegreeSingleCell. For the images shown in the figures, fluorescent image
589 background subtraction was done using Fiji(Schindelin *et al*, 2012) and a sliding
590 paraboloid with rolling ball radius of 50 pixels. Cell signal intensity profiles were generated
591 using Oufti's signal output divided by the total signal intensity to calculate relative signal,
592 which was plotted for individual cells.

593 Relative nucleoid centroid position was extracted from Oufti nucleoid meshes
594 using the MATLAB function get_pole_intensity. The centroid of the nucleoid mesh was
595 calculated and normalized to cell length such that 0 indicates that the nucleoid midpoint
596 is position at the cell center while 0.5 and -0.5 indicate a nucleoid midpoint position at a
597 pole. Nucleoid asymmetry was determined by measuring the absolute distance of the
598 nucleoid midpoint to the cell's centroid, which was then normalized by the cell length.

599 Signal correlation factor (SCF) was calculated as before (Gray *et al*, 2019)
600 excluding the poles (i.e., pixels within 5 pixels from the pole), within a cell width of four
601 pixels along the midline.

602 To analyze constricting cells using the SuperSegger-Omnipose software
603 (https://github.com/tlo-bot/supersegger-omnipose), the software's pre-trained
604 *bact_phase_omni* model (Cutler *et al*, 2022; Stylianidou *et al*, 2016) was retrained
605 because it tended to split cells before cell division was completed based on visual
606 inspection. Model retraining was carried out in two steps. First, images of CJW7606 cells
607 (OD 2.83) grown in M9GluCAAT at 30°C were collected on agarose pads containing

608 M9GluCAAT. Cells from 11 fields of view (each of 2048x2048 pixels, ~100-250 cells per
609 field of view) were segmented using the pre-trained model *bact_phase_omni*. The
610 obtained masks were visually inspected, and when the pre-trained model was splitting
611 cells too early, the cells masks were merged back into one single mask using a custom
612 MATLAB code (LabelsMerge_ConstrictingCells.m). The corrected 2044x2048-pixel
613 images (both phase contrast images and cell masks) were then divided into smaller
614 510x512-pixel images. The dataset was further augmented by performing image rotations
615 (90°, 180°, and 270°), resulting in 704 images. This initial training dataset was then used
616 to retrain Omnipose from scratch (with parameters: n_epochs = 4000; tyx = 224,224;
617 batch_size = 16; learning_rate = 0.1, see details in https://omnipose.readthedocs.io) to
618 generate a preliminary model. In the second step, the retrained model was used to re-
619 segment the publicly available *bact_phase* training dataset (https://osf.io/xmury/) that was
620 originally used to train *bact_phase_omni*, including additional images of cells with
621 extreme phenotypes (e.g., with bright intracellular regions in phase contrast images).
622 This generated a larger dataset with a broad spectrum of cell morphologies. The
623 obtained segmented images were then manually curated to eliminate poorly segmented
624 cells. Finally, both training datasets (the first one created in-house, and the one re-
625 segmented from *bact_phase*) were used to retrain Omnipose from scratch (n = 1249
626 images, with parameters: n_epochs = 4000; tyx = 224,224 ; batch_size = 16;
627 learning_rate = 0.1). The resultant model (merge_model_omni) and the Python code
628 used for curating (screening_good_bad.py) and generating the training datasets
629 (generate_training_dataset.py) are available on GitHub

630 (https://github.com/JacobsWagnerLab/published/tree/master/Thappeta_Canas-
631 Duarte_et_al_2024).
632 The correlation between polar glycogen accumulations and the offset of the
633 nucleoid was then analyzed from snapshot images of CJW7606 cells (OD 2.83) that were
634 segmented using a combination of SuperSegger-Omnipose and a MATLAB script
635 (PostSGO_GlycogenSensorAllCells_20240312.m), in which the mid-cell axis of each cell
636 was calculated using a bivariate fit to the distance matrix and used to identify the location
637 of the cell centroid. Fluorescent signals from the glycogen sensor and HU-mCherry were
638 used to segment the areas of glycogen accumulation and the nucleoid, respectively. The
639 difference between the glycogen sensor area for each cell pole was then calculated.
640 Nucleoid offset was determined from the distance between the nucleoid centroid and the
641 cell center. The Spearman correlation coefficient between the two variables was
642 calculated and the contour plot was plotted using a MATLAB script
643 (ContourPlot_20240312.m).
644 To examine the correlation between glycogen accumulation and asymmetric
645 division, constricting cells in transition phase were identified, curated, and analyzed using
646 a custom MATLAB code (PostSGO_GlycogenSensorConstriction_20240312.m). In
647 short, the mid-cell axis of each cell was calculated as before and was used to identify the
648 location of the cell constriction plane. Fluorescence signal was extracted from each cell
649 half (the future daughter cells) and used to create a mask for the glycogen sensor signal,
650 and thus determine the area of the cell occupied by glycogen. The difference between
651 both the area of each future cell and the area occupied by glycogen sensor signal were
652 used to calculate the Spearman correlation coefficient between the two variables.

653 Principal components regression was used to calculate the linear regression shown in Fig
654 6B.
655 To calculate the statistics of the percent change in cell area (100%*((WT-
656 Δ*glgBXCAP)* /Δ*glgBXCAP*)) for each culture in the competition experiment (Fig 6D), mean
657 areas were bootstrapped from the full distribution of areas (n = 500 samplings) and used
658 to calculate the percent change. Means and standard deviations were then calculated
659 from the resulting distributions of fold changes. This analysis was performed using the
660 OutfiDATA_Bootstrap.m script.
661 The degrees of both constriction position and nucleoid centroid asymmetry in the
662 WT and Δ*glgBXCAP* strains were analyzed for each transition phase mix with a MATLAB
663 code (PostSGO_MixesConstriction_20240312.m). For this analysis, constricting cells
664 were identified as described above using the mid-cell axis to determine the constriction
665 position and the cell centroid. The HU-mCherry signal in each constricting cell was used
666 to segment the nucleoid and calculate its centroid. The offsets between the constriction
667 position and the cell centroid, and between the nucleoid centroid and the cell center were
668 calculated and normalized by the length for each constricting cell. The Spearman
669 correlation coefficient and the isocontours were then calculated between the relevant
670 variables.
671
672 **Whole-cell NMR sample preparation and solid-state NMR measurements**
673 Overnight cultures of each bacterial strain were prepared and diluted at least 10,000-fold
674 into 300 mL of the appropriate fresh medium in a 1L flask. To achieve similar final
675 quantities of biomass, two flasks were prepared identically for exponential phase cultures

676 and one flask was prepared for the higher cell density transition-phase samples. Cells
677 were pelleted by centrifugation at 10,000 *g* at 4°C for 10 min and washed twice in cold
678 PBS. Each final sample cell pellet was collected in a 50 mL tube, stored at -80°C, and
679 subsequently lyophilized and packed into a magic-angle spinning NMR rotor.

680 Solid-state ^{13}C CPMAS NMR (Schaefer & Stejskal, 1976) experiments were
681 performed using an 89-mm bore 11.7 T magnet (Agilent Technologies) with an Agilent
682 triple resonance BioMAS probe and DD2 console (Agilent Technologies). Samples were
683 spun at 7143 ± 3 Hz at room temperature in thin-walled (36 µL capacity) 3.2 mm outer
684 diameter zirconia rotors. Cross polarization (CP) was performed with a ^{13}C field strength
685 of 50 kHz and a ^{1}H field strength centered at 57kz with a 10% ramp for the contact time
686 of 1.5 ms. ^{1}H decoupling was performed with two-pulse phase-modulated (TPPM)
687 (Bennett *et al*, 1995) decoupling at 83 kHz. All CPMAS experiments were obtained using
688 a recycle delay of 2 s. Free induction decays were processed using 80 Hz exponential
689 line broadening prior to Fourier transformation. Spectrometer chemical shift referencing
690 was performed by setting the high frequency adamantane peak to 38.5 ppm (Morcombe
691 & Zilm, 2003).

692

693 **Intracellular salts buffer**

694 To mimic the ionic strength of the *E. coli* cytoplasm, a potassium phosphate buffer (PPB)
695 was prepared and supplemented with the appropriate concentrations of intracellular salts.
696 For this, 200 mL of 1 M stock PPB (pH = 7.5) was prepared by mixing 25.63 g of K_2HPO_4
697 and 7.2 g of KH_2PO_4 in MilliQ water. For the intracellular salts buffer (referred to also as
698 IS buffer), a 5X stock was prepared by mixing the 1 M PPB stock to a final 200 mM

699 concentration with 0.425 M NaCl, 1.25 M KCl, 12.5 mM $MgCl_2$ and 0.5 mM $CaCl_2$
700 (Alatossava *et al*, 1985; Gangola & Rosen, 1987; Schultz *et al*, 1962; Szatmári *et al*,
701 2020).
702
703 **Dynamic light scattering measurements**
704 The hydrodynamic diameter of purified mussel glycogen (Sigma-Aldrich 361507-1ML)
705 and commercially available PEG/PEO particles of different molecular weights were
706 measured using a NanoBrook Omni device. 30% w/v stock solutions of PEG1500 (Sigma-
707 Aldrich 81210-500G), PEG3000 (Sigma-Aldrich 8190151000), PEG4000 (Hampton
708 Research HR2-605), PEG6000 (Sigma-Aldrich 81253-250G), PEG8000 (Sigma-Aldrich
709 89510-250G-F), PEG10000 (Sigma-Aldrich 81280-1KG), PEG20000 (ThermoFisher
710 A17925.0B), and PEG35000 (Sigma-Adrich 81310-1KG) were prepared in MilliQ water.
711 5% and 2.5% w/v stock solutions were made of PEO100000 (Sigma-Aldrich 181986-
712 250G) and PEG1000000 (Sigma-Aldrich 372781-250G), respectively. When needed,
713 solutions were incubated at 42°C for 1 hour to help homogenization.
714 For measurements, samples were diluted to a final volume of 10 mL to generate a
715 final concentration of 6% (1.5 kDa PEG and 3 kDa PEG), 3% (4 kDa PEG) ,1.5% (6 kDa
716 PEG, 8 kDa PEG, 10 kDa PEG, 20 kDa PEG and 35 kDa PEG), 0.25% (PEO 100 kDA)
717 or 0.025% PEO 1MDa in either MilliQ water (pH = 6.5) or in the 1X IS buffer (pH = 7.0).
718 Dilutions of the samples were made to ensure that measurements with each PEG/PEO
719 crowder were done with concentrations below their overlap concentrations to avoid self-
720 crowding artifacts in our measurements (de Gennes & Witten, 1980; Julius *et al*, 2019;
721 Smith *et al*, 2023). The hydrodynamic diameter of glycogen was measured in the same

722 IS buffer at a concentration of 2 g/L. To remove dust or other particles that could affect
723 the measurements, all samples were double filtered, first with a 0.22 µm filter followed by
724 a 0.1 µm filter. Each sample (1 mL) was loaded in a cuvette and sealed with a lid. Samples
725 were measured in triplicate for 300 ms at 25°C using a 90-degree angle for the detector.
726

727 **In vitro phase separation experiments**

728 To generate the presented phase diagram, phase separation was assessed using varying
729 concentrations of both glycogen (2.5 to 10 g/L) and 3 kDa PEG (8 to 30 mM). Samples
730 were prepared in the IS buffer to a final volume of 50 µL in 200 µL Eppendorf tubes. For
731 visualization, 0.05 µg/µL of FITC-ConA (Sigma-Aldrich C7642-2MG) was added to the
732 appropriate glycogen volume prior to the addition of other components of the reaction.
733 The appropriate volume of 3 kDa PEG was added last, and a 12 µL aliquot was
734 immediately transferred to a 50 x 7mm glass bottom dish (PELCO) for imaging at 25°C.

735 To determine the minimal concentration of PEG/PEO that promotes glycogen
736 LLPS, samples were prepared as described above with 9 g/L of glycogen. Increasing
737 concentrations of each PEG (1.5 to 35 kDa) or PEO (100 kDa and 1 MDa) were tested in
738 50 µL reactions. Each sample (12 µL) was imaged by phase contrast microscopy (100x
739 Ph3 objective) to visually assess if glycogen condensates appeared. The smallest
740 concentration at which the reactions transitioned from one phase to another was assigned
741 as the minimal concentration. For PEO 1MDa, the minimal concentration required to drive
742 LLPS was found to be above the overlap concentration (0.5% w/v) reported for this
743 polymer (Smith *et al*, 2023), which marks the onset of “self-crowding”. Therefore, the
744 hydrodynamic diameter of the polymer above this concentration could not be determined

745 using DSL. Unless otherwise indicated, all experiments were conducted and imaged at
746 25°C.
747
748 **In vitro experiments showing protein probe exclusion by glycogen condensates**
749 For the fluorescent protein exclusion assay, glass bottom dishes were cleaned using 1mL
750 of 100% isopropanol, then washed twice with 90% ethanol and allowed to dry completely.
751 Dishes were then treated with Pluronic® F-108 (Sigma-Aldrich 542342-250G) to minimize
752 fluorescent protein binding to the glass. Briefly, 200 µL of IS buffer supplemented with
753 0.1% w/v Pluronic® F-108 was pipetted into the dish and allowed to incubate for 1 h,
754 followed by two washes with 200 µL of IS buffer. All remaining liquid was removed and
755 the dish was allowed to dry completely. Phase separation reactions were made to final
756 concentrations of 10 g/L of glycogen, 1X IS buffer, 15 µM GFP (ThermoFisher A42613)
757 or mCherry (Abcam AB199750), and 20 mM 3 kDa PEG as described above. Samples
758 (12 µL) were imaged at 25°C, 30°C, and 37°C. For imaging, the focal plane was set on
759 the surface of the glass to minimize background signal from the column of liquid around
760 the condensates (Fig 5I), except for the images shown in Video EV4 for which images
761 were taken as a z-stack (with 0.125 µm steps) above the glass surface. For the images
762 shown in the figures, fluorescent image background subtraction was done using
763 Fiji(Schindelin *et al*, 2012) and a sliding paraboloid with rolling ball radius of 50 pixels.
764
765 **Co-culture experiments**
766 Cells of four strains (CJW7665-7668), each expressing a different fluorescent protein in
767 either the glycogen-devoid mutant strain or its WT parent, were inoculated in 2 mL of

768 M9GluCAAT and grown overnight at 30°C with 220 rpm shaking. Each culture was then
769 diluted 1:10,000 into fresh 2 mL cultures and returned to the shaker until they reached an
770 OD ~0.1. Samples of WT and glycogen-devoid strains were mixed proportional to their
771 ODs to create a ~50:50 mixture. For these experiments, two types of mixtures were used:
772 one included WT cells expressing mSCFP3 and mutant cells expressing mVenus, while
773 the other included WT cells expressing mVenus and mutant cells expressing mSCFP3.
774 Mixtures were made independently in three biological replicates. Each mixture was then
775 diluted 1:10,000 into 50 mL of medium in a 250 mL flask and returned to the shaker.
776 Samples were taken at OD 2.6 for transition phase. Samples were prepared for imaging
777 on agarose pads as described above.
778

779 **DATA AVAILABILITY**

780 Image analysis code and the newly trained segmentation model for images of *E. coli* cells
781 on agarose pads are available on the Jacobs-Wagner lab Github repository
782 (https://github.com/JacobsWagnerLab/published/tree/master/Thappeta_Canas-
783 Duarte_et_al_2024).
784

785 **AUTHOR CONTRIBUTIONS**

786 Y.T., S.J.C.-D, and C.J.-W prepared the manuscript and conceptualized the study. W.G.
787 and C.L. collected preliminary observations and data. YT, S.J.C-D and C.J.-W designed
788 in vivo experiments. Y.T. and S.J.C.-D performed in vivo experiments. S.J.C.-D and C.J.-
789 W designed in vitro experiments. S.J.C.-D performed in vitro experiments and constructed
790 the glycogen biosensor. S.J.C.-D and Y.X. developed analysis pipeline. S.J.C.-D and A.F.

optimized Omnipose segmentation model for analysis. S.J.C.-D, and Y.T. analyzed data. T.K. and L.C. performed and analyzed whole cell NMR experiments. L.C and C.J.-W provided supervision, project administration, and funding acquisition.

ACKNOWLEDGMENTS

We are grateful to Dr. Johan Paulsson for sharing unpublished strains used in this study. We thank Drs. Suckjoon Jun and KC Huang for sharing published strains, and Dr. Sangjin Kim for generating a P1 transduction that generated strain CJW5685. We are thankful to Drs. Onn Brandman, KC Huang, and Jonas Cremer for valuable discussion. Finally, we express our gratitude to the Jacobs-Wagner laboratory for support, discussion, and critical reading of the manuscript. Part of this work was performed at the Stanford Nano Shared Facilities (SNSF), supported by the National Science Foundation under award ECCS-2026822. This research was supported in part by the Netherlands Organization for Scientific Research (NWO), Rubicon 2022-2 Science programme, 019.222EN.001 (A.F.), and the National Institutes of Health grant R01GM117278 (L.C.). C.J.-W. is an investigator of the Howard Hughes Medical Institute.

DISCLOSURE AND COMPETING INTERESTS STATEMENT

The authors declare no competing interests.

810 **REFERENCES**

811 Åkerlund T, Nordstro¨m K, Nordstro¨m N & Bernander R (1995) Analysis of Cell Size and
812 DNA Content in Exponentially Growing and Stationary-Phase Batch Cultures of
813 Escherichia coli. *J Bacteriol* 177: 6791–6797

814 Alatossava T, Jütte H, Kuhn A & Kellenberger E (1985) Manipulation of intracellular
815 magnesium content in polymyxin B nonapeptide-sensitized Escherichia coli by
816 ionophore A23187. *J Bacteriol* 162: 413–419

817 Alberti S, Gladfelter A & Mittag T (2019) Considerations and Challenges in Studying
818 Liquid-Liquid Phase Separation and Biomolecular Condensates. *Cell* 176: 419–434
819 doi:10.1016/j.cell.2018.12.035 [PREPRINT]

820 Alberti S & Hyman AA (2021) Biomolecular condensates at the nexus of cellular stress,
821 protein aggregation disease and ageing. *Nat Rev Mol Cell Biol* 22: 196–213

822 Alberti S, Saha S, Woodruff JB, Franzmann TM, Wang J & Hyman AA (2018) A User's
823 Guide for Phase Separation Assays with Purified Proteins. *J Mol Biol* 430: 4806–
824 4820

825 Albi T & Serrano A (2016) Inorganic polyphosphate in the microbial world. Emerging roles
826 for a multifaceted biopolymer. *World J Microbiol Biotechnol* 32: 27

827 Almagro G, Viale AM, Montero M, Rahimpour M, Muñoz FJ, Baroja-Fernández E, Bahaji
828 A, Zúñiga M, González-Candelas F & Pozueta-Romero J (2015) Comparative
829 genomic and phylogenetic analyses of gammaproteobacterial glg genes traced the
830 origin of the Escherichia coli glycogen glgBXCAP operon to the last common
831 ancestor of the sister orders Enterobacteriales and Pasteurellales. *PLoS One* 10

832 Alonso-Casajús N, Dauvillée D, Viale AM, Muñoz FJ, Baroja-Fernández E, Morán-
833 Zorzano MT, Eydallin G, Ball S & Pozueta-Romero J (2006) Glycogen
834 phosphorylase, the product of the glgP gene, catalyzes glycogen breakdown by
835 removing glucose units from the nonreducing ends in Escherichia coli. *J Bacteriol*
836 188: 5266–5272
837 Amselem E, Broadwater B, Hävermark T, Johansson M & Elf J (2023) Real-time single-
838 molecule 3D tracking in E. coli based on cross-entropy minimization. *Nat Commun*
839 14: 1–11
840 Asakura S & Oosawa F (1954) On Interaction between Two Bodies Immersed in a
841 Solution of Macromolecules. *J Chem Phys* 22: 1255–1256
842 Asakura S & Oosawa F (1958) Interaction between particles suspended in solutions of
843 macromolecules. *Journal of Polymer Science* 33: 183–192
844 Azaldegui CA, Vecchiarelli AG & Biteen JS (2021) The emergence of phase separation
845 as an organizing principle in bacteria. *Biophys J* 120: 1123–1138
846 Azam TA, Hiraga S & Ishihama A (2000) Two types of localization of the DNA-binding
847 proteins within the Escherichia coli nucleoid. *Genes to Cells* 5: 613–626
848 Badrinarayanan A, Lesterlin C, Reyes-Lamothe R & Sherratt D (2012) The Escherichia
849 coli SMC Complex, MukBEF, Shapes Nucleoid Organization Independently of DNA
850 Replication. *J Bacteriol* 194: 4669–4676
851 Bakshi S, Choi H, Mondal J & Weisshaar JC (2014) Time-dependent effects of
852 transcription- and translation-halting drugs on the spatial distributions of the E
853 scherichia coli chromosome and ribosomes. *Mol Microbiol* 94: 871–887

854 Bakshi S, Leoncini E, Baker C, Cañas-Duarte SJ, Okumus B & Paulsson J (2021)
855 Tracking bacterial lineages in complex and dynamic environments with applications
856 for growth control and persistence. *Nature Microbiology 2021 6:6* 6: 783–791
857 Bakshi S, Siryaporn A, Goulian M & Weisshaar JC (2012) Superresolution imaging of
858 ribosomes and RNA polymerase in live Escherichia coli cells. *Mol Microbiol* 85: 21–
859 38
860 Baldwin WW, Myer R, Powell N, Anderson E & Koch AL (1995) Buoyant density of
861 Escherichia coli is determined solely by the osmolarity of the culture medium. *Arch*
862 *Microbiol* 164: 155–7
863 Balleza E, Kim JM & Cluzel P (2018) Systematic characterization of maturation time of
864 fluorescent proteins in living cells. *Nat Methods* 15: 47–51
865 Banani SF, Lee HO, Hyman AA & Rosen MK (2017) Biomolecular condensates:
866 Organizers of cellular biochemistry. *Nat Rev Mol Cell Biol* 18: 285–298
867 Bates D & Kleckner N (2005) Chromosome and replisome dynamics in E. coli: Loss of
868 sister cohesion triggers global chromosome movement and mediates chromosome
869 segregation. *Cell* 121: 899–911
870 Becker JW, Reeke GN, Cunningham BA & Edelman GM (1976) New evidence on the
871 location of the saccharide-binding site of concanavalin A. *Nature* 259: 406–409
872 Bennett AE, Rienstra CM, Auger M, Lakshmi K V. & Griffin RG (1995) Heteronuclear
873 decoupling in rotating solids. *J Chem Phys* 103: 6951–6958
874 Bezborodkina NN, Chestnova AY, Vorobev ML & Kudryavtsev BN (2018) Spatial
875 Structure of Glycogen Molecules in Cells. *Biochemistry (Moscow)* 83: 467–482

876 Boehm A, Arnoldini M, Bergmiller T, Röösli T, Bigosch C & Ackermann M (2016) Genetic
877 Manipulation of Glycogen Allocation Affects Replicative Lifespan in E. coli. *PLoS*
878 *Genet* 12
879 Boeynaems S, Alberti S, Fawzi NL, Mittag T, Polymenidou M, Rousseau F, Schymkowitz
880 J, Shorter J, Wolozin B, Van Den Bosch L, *et al* (2018) Protein Phase Separation: A
881 New Phase in Cell Biology. *Trends Cell Biol* 28: 420–435
882 Bourassa L & Camilli A (2009) Glycogen contributes to the environmental persistence
883 and transmission of Vibrio cholerae. *Mol Microbiol* 72: 124–38
884 Brandt F, Etchells SA, Ortiz JO, Elcock AH, Hartl FU & Baumeister W (2009) The Native
885 3D Organization of Bacterial Polysomes. *Cell* 136: 261–271
886 Bremer H & Dennis PP (2008) Modulation of Chemical Composition and Other
887 Parameters of the Cell at Different Exponential Growth Rates. *EcoSal Plus* 3
888 Buchanan RE (1918) Life Phases in a Bacterial Culture
889 Chai Q, Singh B, Peisker K, Metzendorf N, Ge X, Dasgupta S & Sanyal S (2014)
890 Organization of Ribosomes and Nucleoids in Escherichia coli Cells during Growth
891 and in Quiescence. *Journal of Biological Chemistry* 289: 11342–11352
892 Chen YJ, Liu P, Nielsen AAK, Brophy JAN, Clancy K, Peterson T & Voigt CA (2013)
893 Characterization of 582 natural and synthetic terminators and quantification of their
894 design constraints. *Nature Methods 2013 10:7* 10: 659–664
895 Cherepanov PP & Wackernagel W (1995) Gene disruption in Escherichia coli: TcR and
896 KmR cassettes with the option of Flp-catalyzed excision of the antibiotic-resistance
897 determinant. *Gene* 158: 9–14

898 Cohan MC & Pappu R V. (2020) Making the Case for Disordered Proteins and
899 Biomolecular Condensates in Bacteria. *Trends Biochem Sci* 45: 668–680
900 Cutler KJ, Stringer C, Lo TW, Rappez L, Stroustrup N, Brook Peterson S, Wiggins PA &
901 Mougous JD (2022) Omnipose: a high-precision morphology-independent solution
902 for bacterial cell segmentation. *Nature Methods 2022 19:11* 19: 1438–1448
903 Datsenko KA & Wanner BL (2000) One-step inactivation of chromosomal genes in
904 Escherichia coli K-12 using PCR products. *Proc Natl Acad Sci U S A* 97: 6640–5
905 Devanand K & Selser JC (1991) Asymptotic behavior and long-range interactions in
906 aqueous solutions of poly(ethylene oxide). *Macromolecules* 24: 5943–5947
907 Diner EJ, Garza-Sánchez F & Hayes CS (2011) Genome Engineering Using Targeted
908 Oligonucleotide Libraries and Functional Selection. In *Bone*, Williams JA (ed) pp 71–
909 82. Totowa, NJ: Humana Press
910 Dworkin J & Harwood CS (2022) Metabolic Reprogramming and Longevity in
911 Quiescence. *Annu Rev Microbiol* 76: 91–111
912 Elowitz MB, Surette MG, Wolf P-E, Stock JB & Leibler S (1999) Protein Mobility in the
913 Cytoplasm of *Escherichia coli*. *J Bacteriol* 181: 197–203
914 Erickson HP (2009) Size and shape of protein molecules at the nanometer level
915 determined by sedimentation, gel filtration, and electron microscopy. *Biol Proced*
916 *Online* 11: 32–51 doi:10.1007/s12575-009-9008-x [PREPRINT]
917 Feijó Delgado F, Cermak N, Hecht VC, Son S, Li Y, Knudsen SM, Olcum S, Higgins JM,
918 Chen J, Grover WH, *et al* (2013) Intracellular Water Exchange for Measuring the Dry
919 Mass, Water Mass and Changes in Chemical Composition of Living Cells. *PLoS One*
920 8: e67590

921 Floc'h K, Lacroix F, Servant P, Wong Y-S, Kleman J-P, Bourgeois D & Timmins J (2019)
922 Cell morphology and nucleoid dynamics in dividing Deinococcus radiodurans. *Nat*
923 *Commun* 10: 3815
924 Gangola P & Rosen BP (1987) Maintenance of intracellular calcium in Escherichia coli.
925 *Journal of Biological Chemistry* 262: 12570–12574
926 de Gennes PG & Witten TA (1980) *Scaling Concepts in Polymer Physics*. *Phys Today*
927 33: 51–54
928 Govers SK, Campos M, Tyagi B, Laloux G & Jacobs-Wagner C (2024) Apparent simplicity
929 and emergent robustness in the control of the Escherichia coli cell cycle. *Cell Syst*
930 15: 19-36.e5
931 Govons S, Vinopal R, Ingraham J & Preiss J (1969) Isolation of mutants of Escherichia
932 coli B altered in their ability to synthesize glycogen. *J Bacteriol* 97: 970–972
933 Gray W, Govers SK, Xiang Y, Parry BR, Campos M, Kim S & Jacobs-Wagner
934 Correspondence C (2019) Nucleoid Size Scaling and Intracellular Organization of
935 Translation across Bacteria Nucleoid size scaling Continuum of NC ratios across
936 species NC ratio. *Cell* 177: 1632-1648.e20
937 Gründel M, Scheunemann R, Lockau W & Zilliges Y (2012) Impaired glycogen synthesis
938 causes metabolic overflow reactions and affects stress responses in the
939 cyanobacterium Synechocystis sp. PCC 6803. *Microbiology (United Kingdom)* 158:
940 3032–3043
941 Hedge PJ & Spratt BG (1985) Resistance to β-lactam antibiotics by re-modelling the
942 active site of an E. coli penicillin-binding protein. *Nature 1985 318:6045* 318: 478–
943 480

944 Henrissat B, Deleury E & Coutinho PM (2002) Glycogen metabolism loss: a common
945 marker of parasitic behaviour in bacteria? *Trends in Genetics* 18: 437–440
946 Hink MA, Griep RA, Borst JW, van Hoek A, Eppink MHM, Schots A & Visser AJWG (2000)
947 Structural Dynamics of Green Fluorescent Protein Alone and Fused with a Single
948 Chain Fv Protein. *Journal of Biological Chemistry* 275: 17556–17560
949 Hoang AY, Azaldegui CA, Ghalmi M, Biteen JS & Vecchiarelli AG (2023) An experimental
950 framework to assess biomolecular condensates in bacteria.
951 Holme T, Laurent T, Palmstierna H, Magnéli A, Magnéli A, Pestmalis H & Åsbrink S (1957)
952 On the Glycogen in Escherichia coli B; Variations in Molecular Weight during Growth.
953 I. *Acta Chem Scand* 11: 757–762
954 Holme T, Palmstierna H, Ulfvarson U, Stenhagen E & Thorell B (1956) Changes in
955 Glycogen and Nitrogen-containing Compounds in Escherichia coli B during Growth
956 in Deficient Media. I. Nitrogen and Carbon Starvation. *Acta Chem Scand* 10: 578–
957 586
958 Hyman AA, Weber CA & Jülicher F (2014) Liquid-liquid phase separation in biology. *Annu*
959 *Rev Cell Dev Biol* 30: 39–58 doi:10.1146/annurev-cellbio-100913-013325
960 [PREPRINT]
961 Ingraham JL, Maaløe O & Neidhardt FC (1983) Growth of the bacterial cell Sunderland
962 (Mass.) : Sinauer associates
963 Jensen KF (1993) The Escherichia coli K-12 ‘wild types’ W3110 and MG1655 have an
964 rph frameshift mutation that leads to pyrimidine starvation due to low pyrE expression
965 levels. *J Bacteriol* 175: 3401–3407

966 Jones SA, Jorgensen M, Chowdhury FZ, Rodgers R, Hartline J, Leatham MP, Struve C,
967 Krogfelt KA, Cohen PS & Conway T (2008) Glycogen and Maltose Utilization by
968 Escherichia coli O157:H7 in the Mouse Intestine. *Infect Immun* 76: 2531
969 Julius K, Weine J, Gao M, Latarius J, Elbers M, Paulus M, Tolan M & Winter R (2019)
970 Impact of Macromolecular Crowding and Compression on Protein-Protein
971 Interactions and Liquid-Liquid Phase Separation Phenomena. *Macromolecules* 52:
972 1772–1784
973 Khemici V, Poljak L, Luisi BF & Carpousis AJ (2008) The RNase E of Escherichia coli is
974 a membrane-binding protein. *Mol Microbiol* 70: 799–813
975 Klotz A & Forchhammer K (2017) Glycogen, a major player for bacterial survival and
976 awakening from dormancy. *Future Microbiol* 12: 101–104
977 Klotz A, Georg J, Bučinská L, Watanabe S, Reimann V, Januszewski W, Sobotka R,
978 Jendrossek D, Hess WR & Forchhammer K (2016) Awakening of a Dormant
979 Cyanobacterium from Nitrogen Chlorosis Reveals a Genetically Determined
980 Program. *Current Biology* 26: 2862–2872
981 Konopka MC, Sochacki KA, Bratton BP, Shkel IA, Record MT & Weisshaar JC (2009)
982 Cytoplasmic Protein Mobility in Osmotically Stressed *Escherichia coli*. *J Bacteriol*
983 191: 231–237
984 Kubitschek HE, Baldwin WW & Graetzer R (1983) Buoyant density constancy during the
985 cell cycle of Escherichia coli. *J Bacteriol* 155: 1027–1032
986 Kubitschek HE & Friske JA (1986) Determination of bacterial cell volume with the Coulter
987 Counter. *J Bacteriol* 168: 1466–1467

988 Landgraf D, Okumus B, Chien P, Baker TA & Paulsson J (2012) Segregation of molecules
989 at cell division reveals native protein localization. *Nat Methods* 9: 480–482
990 Li XT, Jun Y, Erickstad MJ, Brown SD, Parks A, Court DL & Jun S (2016) tCRISPRi:
991 tunable and reversible, one-step control of gene expression. *Scientific Reports 2016*
992 *6:1* 6: 1–12
993 Liu Q, Li J, Zhang W, Xiao C, Zhang S, Nian C, Li J, Su D, Chen L, Zhao Q, *et al* (2021a)
994 Glycogen accumulation and phase separation drives liver tumor initiation. *Cell* 184:
995 5559-5576.e19
996 Liu Q-H, Tang J-W, Wen P-B, Wang M-M, Zhang X & Wang L (2021b) From Prokaryotes
997 to Eukaryotes: Insights Into the Molecular Structure of Glycogen Particles. *Front Mol*
998 *Biosci* 8: 1–15
999 Loferer-Krössbacher M, Klima J & Psenner R (1998) Determination of bacterial cell dry
1000 mass by transmission electron microscopy and densitometric image analysis. *Appl*
1001 *Environ Microbiol* 64: 688–94
1002 Lukatsky DB & Shakhnovich EI (2008) Statistically enhanced promiscuity of structurally
1003 correlated patterns. *Phys Rev E* 77: 020901
1004 Lutkenhaus J (2008) Min oscillation in bacteria. *Adv Exp Med Biol* 641: 49–61
1005 Lvov Y, Ariga K, Ichinose I & Kunitake T (1996) Molecular film assembly via layer-by-
1006 layer adsorption of oppositely charged macromolecules (linear polymer, protein and
1007 clay) and concanavalin A and glycogen. *Thin Solid Films* 284–285: 797–801
1008 Madsen NB (1963) The biological control of glycogen metabolism in Agrobacterium
1009 tumefaciens. *Can J Biochem Physiol* 41: 561–571

1010 Milo R (2013) What is the total number of protein molecules per cell volume? A call to
1011 rethink some published values. *BioEssays* 35: 1050–1055
1012 Mohapatra S & Weisshaar JC (2018) Functional mapping of the E. coli translational
1013 machinery using single-molecule tracking. *Mol Microbiol* 110: 262–282
1014 Morcombe CR & Zilm KW (2003) Chemical shift referencing in MAS solid state NMR.
1015 *Journal of Magnetic Resonance* 162: 479–486
1016 Morita RY (1990) The starvation-survival state of microorganisms in nature and its
1017 relationship to the bioavailable energy. *Experientia* 46: 813–817
1018 Mulder EG, Deinema MH, van Veen WL & Zevenhuizen LPTM (1962) Polysaccharides,
1019 lipids and poly-β-hydroxybutyrate in microorganisms. *Recueil des Travaux*
1020 *Chimiques des Pays-Bas* 81: 797–809
1021 Neidhardt FC & Curtiss R (1996) Escherichia coli and Salmonella : cellular and molecular
1022 biology
1023 Nilsson M, Bülow L & Wahlund K-G (1997) Use of flow field-flow fractionation for the rapid
1024 quantitation of ribosome and ribosomal subunits inEscherichia coli at different protein
1025 production conditions. *Biotechnol Bioeng* 54: 461–467
1026 Nyström T (2004) Stationary-Phase Physiology. *Annu Rev Microbiol* 58: 161–181
1027 Nyström T & Kjelleberg S (1989) Role of Protein Synthesis in the Cell Division and
1028 Starvation Induced Resistance to Autolysis of a Marine Vibrio during the Initial Phase
1029 of Starvation. *Microbiology (N Y)* 135: 1599–1606
1030 Paintdakhi A, Parry B, Campos M, Irnov I, Elf J, Surovtsev I & Jacobs-Wagner C (2016)
1031 Oufti: an integrated software package for high-accuracy, high-throughput quantitative
1032 microscopy analysis. *Mol Microbiol* 99: 767–77

1033 Pelletier JF, Field CM, Coughlin M, Ryazanova L, Sonnett M, Wühr M & Mitchison TJ
1034 (2021) Glycogen-dependent demixing of frog egg cytoplasm at increased crowding.
1035 1–21
1036 Persson LB, Ambati VS & Brandman O (2020) Cellular Control of Viscosity Counters
1037 Changes in Temperature and Energy Availability. *Cell* 183: 1572-1585.e16
1038 Phillips LA, Hotham-Iglewski B & Franklin RM (1969) Polyribosomes of Escherichia coli:
1039 II. Experiments to determine the in vivo distribution of polysomes, ribosomes and
1040 ribosomal subunits. *J Mol Biol* 45: 23–38
1041 Pogliano J, Pogliano K, Weiss DS, Losick R & Beckwith J (1997) Inactivation of FtsI
1042 inhibits constriction of the FtsZ cytokinetic ring and delays the assembly of FtsZ rings
1043 at potential division sites
1044 Potma EO, De Boeij WP, Bosgraaf L, Roelofs J, Van Haastert PJM & Wiersma DA (2001)
1045 Reduced Protein Diffusion Rate by Cytoskeleton in Vegetative and Polarized
1046 Dictyostelium Cells. *Biophys J* 81: 2010–2019
1047 Preiss J (1984) Bacterial glycogen synthesis and its regulation. *Annu Rev Microbiol* 38:
1048 419–58
1049 Preiss J & Romeo T (1990) Physiology, Biochemistry and Genetics of Bacterial Glycogen
1050 Synthesis. In pp 183–238.
1051 Preiss J & Romeo T (1994) Molecular biology and regulatory aspects of glycogen
1052 biosynthesis in bacteria. *Prog Nucleic Acid Res Mol Biol* 47: 299–329
1053 Racki LR, Tocheva EI, Dieterle MG, Sullivan MC, Jensen GJ & Newman DK (2017)
1054 Polyphosphate granule biogenesis is temporally and functionally tied to cell cycle exit

1055 during starvation in Pseudomonas aeruginosa. *Proc Natl Acad Sci U S A* 114:
1056 E2440–E2449
1057 Rolinson GN (1980) Effect of beta-lactam antibiotics on bacterial cell growth rate. *J Gen*
1058 *Microbiol* 120: 317–323
1059 Rostam N, Ghosh S, Chow CFW, Hadarovich A, Landerer C, Ghosh R, Moon HK,
1060 Hersemann L, Mitrea DM, Klein IA, *et al* (2023) CD-CODE: crowdsourcing
1061 condensate database and encyclopedia. *Nat Methods* 20: 673–676
1062 Sanamrad A, Persson F, Lundius EG, Fange D, Gynnå AH & Elf J (2014) Single-particle
1063 tracking reveals that free ribosomal subunits are not excluded from the Escherichia
1064 coli nucleoid. *Proc Natl Acad Sci U S A* 111: 11413–11418
1065 Schaefer J & Stejskal EO (1976) Carbon-13 Nuclear Magnetic Resonance of Polymers
1066 Spinning at the Magic Angle. *J Am Chem Soc* 98: 1031–1032
1067 Schavemaker PE, Śmigiel WM & Poolman B (2017) Ribosome surface properties may
1068 impose limits on the nature of the cytoplasmic proteome. *Elife* 6
1069 Schindelin J, Arganda-Carreras I, Frise E, Kaynig V, Longair M, Pietzsch T, Preibisch S,
1070 Rueden C, Saalfeld S, Schmid B, *et al* (2012) Fiji: An open-source platform for
1071 biological-image analysis. *Nat Methods* 9: 676–682
1072 Schultz SG, Wilson NL & Epstein W (1962) Cation Transport in Escherichia coli. *Journal*
1073 *of General Physiology* 46: 159–166
1074 Sekar K, Linker SM, Nguyen J, Grünhagen A, Stocker R & Sauer U (2020) Bacterial
1075 Glycogen Provides Short-Term Benefits in Changing Environments. *Appl Environ*
1076 *Microbiol* 86

1077 Sharp KA (2015) Analysis of the size dependence of macromolecular crowding shows
1078 that smaller is better. *Proc Natl Acad Sci U S A* 112: 7990–7995
1079 Sherratt DJ (2003) Bacterial chromosome dynamics. *Science (1979)* 301: 780–785
1080 Shi H, Westfall CS, Kao J, Odermatt PD, Anderson SE, Cesar S, Sievert M, Moore J,
1081 Gonzalez CG, Zhang L, *et al* (2021) Starvation induces shrinkage of the bacterial
1082 cytoplasm. *Proc Natl Acad Sci U S A* 118: 2104686118
1083 Shih YL & Zheng M (2013) Spatial control of the cell division site by the Min system in
1084 Escherichia coli. *Environ Microbiol* 15: 3229–3239
1085 Shively JM (1974) Inclusion Bodies of Prokaryotes. *Annu Rev Microbiol* 28: 167–188
1086 Sigal N, Cattaneo J & Segel IH (1964) Glycogen accumulation by wild-type and uridine
1087 diphosphate glucose pyrophosphorylase-negative strains of Escherichia coli. *Arch*
1088 *Biochem Biophys* 108: 440–451
1089 Skurat A V., Segvich DM, Depaoli-Roach AA & Roach PJ (2017) Novel method for
1090 detection of glycogen in cells. *Glycobiology* 27: 416–424
1091 Smith WC, Qu H, Zheng K, Baek JH, Gao Y, Buehler PW, Feng X & Xu X (2023)
1092 Determining critical overlap concentration of polyethylene oxide to support excipient
1093 safety assessment of opioid products. *Int J Pharm* 632
1094 Strahl H, Turlan C, Khalid S, Bond PJ, Kebalo JM, Peyron P, Poljak L, Bouvier M, Hamoen
1095 L, Luisi BF, *et al* (2015) Membrane Recognition and Dynamics of the RNA
1096 Degradosome. *PLoS Genet* 11: e1004961
1097 Strange RE, Dark FA & Ness AG (1961) The Survival of Stationary Phase Aerobacter
1098 aerogenes Stored in Aqueous Suspension. *J Gen Microbiol* 25: 61–76

1099 Stylianidou S, Brennan C, Nissen SB, Kuwada NJ & Wiggins PA (2016) SuperSegger:
1100 robust image segmentation, analysis and lineage tracking of bacterial cells. *Mol*
1101 *Microbiol* 102: 690–700
1102 Surovtsev I V. & Jacobs-Wagner C (2018) Subcellular Organization: A Critical Feature of
1103 Bacterial Cell Replication. *Cell* 172: 1271–1293
1104 Swaminathan R, Hoang CP & Verkman AS (1997) Photobleaching recovery and
1105 anisotropy decay of green fluorescent protein GFP-S65T in solution and cells:
1106 cytoplasmic viscosity probed by green fluorescent protein translational and rotational
1107 diffusion. *Biophys J* 72: 1900–1907
1108 Szatmári D, Sárkány P, Kocsis B, Nagy T, Miseta A, Barkó S, Longauer B, Robinson RC
1109 & Nyitrai M (2020) Intracellular ion concentrations and cation-dependent remodelling
1110 of bacterial MreB assemblies. *Sci Rep* 10: 12002
1111 Thomason LC, Costantino N & Court DL (2007) E. coli Genome Manipulation by P1
1112 Transduction. *Curr Protoc Mol Biol* 79
1113 Wang L, Liu Q, Tan X, Wang Z, Wang M, Wise MJ, Li C, Ma C, Li E, Deng B, *et al* (2019a)
1114 Molecular Structure of Glycogen in Escherichia coli. *Biomacromolecules* 20: 2821–
1115 2829
1116 Wang L & Wise MJ (2011) Glycogen with short average chain length enhances bacterial
1117 durability. *Naturwissenschaften* 98: 719–729
1118 Wang M, Liu Q, Kang X, Zhu Z, Yang H, Xi X, Zhang X, Du Y, Guo M, Tang D, *et al* (2020)
1119 Glycogen Metabolism Impairment via Single Gene Mutation in the glgBXCAP Operon
1120 Alters the Survival Rate of Escherichia coli Under Various Environmental Stresses.
1121 *Front Microbiol* 11

1122 Wang Z, Zhang G & Zhang H (2019b) Protocol for analyzing protein liquid–liquid phase
1123 separation. *Biophys Rep* 5: 1–9
1124 Wilson WA, Roach PJ, Montero M, Baroja-Fernández E, Muñoz FJ, Eydallin G, Viale AM
1125 & Pozueta-Romero J (2010) Regulation of glycogen metabolism in yeast and
1126 bacteria. *FEMS Microbiol Rev* 34: 952–985
1127 Woldringh CL, Mulder E, Valkenburg JAC, Wientjes FB, Zaritsky A & Nanninga N (1990)
1128 Role of the nucleoid in the toporegulation of division. *Res Microbiol* 141: 39–49
1129 Yoshioka K, Saito M, Oh K-B, Nemoto Y, Matsuoka H, Natsume M & Abe H (1996a)
1130 Intracellular Fate of 2-NBDG, a Fluorescent Probe for Glucose Uptake Activity, in
1131 *Escherichia coli* Cells. *Biosci Biotechnol Biochem* 60: 1899–1901
1132 Yoshioka K, Takahashi H, Homma T, Saito M, Oh K-B, Nemoto Y & Matsuoka H (1996b)
1133 A novel fluorescent derivative of glucose applicable to the assessment of glucose
1134 uptake activity of Escherichia coli. *Biochimica et Biophysica Acta (BBA) - General*
1135 *Subjects* 1289: 5–9
1136 Zevenhuizen LPTM (1966) Formation and function of the glycogen-like polysaccharide
1137 ofArthrobacter. *Antonie Van Leeuwenhoek* 32: 356–372
1138 Zhu Y, Fan Z, Wang R, Xie R, Guo H, Zhang M, Guo B, Sun T, Zhang H, Zhuo L, *et al*
1139 (2020) Single-Cell Analysis for Glycogen Localization and Metabolism in Cultured
1140 Astrocytes. *Cell Mol Neurobiol* 40: 801–812
1141
1142

1143 **FIGURE LEGENDS**

1144 **Fig 1: Mean single-cell features change as the cell density of the culture increases.**
1145 Except for panel A for which the same culture was analyzed across the entire growth
1146 curve, samples of different cultures of CJW4677 were collected at 42 different ODs (n >
1147 500 cells for each OD) for cell imaging. Shown are binned data for the indicated OD range,
1148 with the mean describing the averaged mean value for cell samples from three OD values
1149 and error bars indicating the standard deviation. Grey, red, and blue shades indicate
1150 exponential, transition, and stationary phases, respectively.

1151 **A** Growth curves of two independent cultures of strain CJW4677. OD measurements
1152 were manually collected by spectrophotometry over time.

1153 **B** Scatter plot of OD vs. mean cell area.

1154 **C** Same as panel B but for mean number of nucleoids per cell.

1155 **D** Scatter plot of OD vs. fraction of cells with one nucleoid.

1156 **E** Same as panel D but for the fraction of constricting cells in the population.

1157 **F** Scatter plot of OD vs. mean division asymmetry, which was calculated by dividing the
1158 absolute distance of the division position from the cell center by cell length and averaging
1159 across cells. This was done for cultures at ODs at which the fraction of dividing cells in
1160 the population was greater than 0.05.

1161 **G** Scatter plot of OD vs mean nucleoid asymmetry, which was determined by calculating
1162 the absolute distance between the nucleoid mid-point and cell center, normalized for cell
1163 length. Note that for cells with two nucleoids, their relative mid-points were averaged such
1164 that when the center of each nucleoid was positioned at the relative quarter cell positions,
1165 the mean mid-point was at the cell center.

1166 **Fig 2: The localization pattern of cytoplasmic components changes in transition**
1167 **phase.**
1168 **A** Representative phase contrast and fluorescence images of DAPI-labeled CJW7325
1169 cells expressing RplA-mCherry and msfGFP, along with corresponding cell signal
1170 intensity profiles. Cultures were in exponential phase (OD 0.14) or transition phase (OD
1171 1.83), as indicated. Fluorescence intensity is indicated in arbitrary units (a.u.). Scale bar:
1172 2 μm
1173 **B** Distributions of signal correlation factor (SCF) values between DAPI and RplA-mCherry
1174 for exponential (n = 1242 cells) and transition (n = 1444 cells) phases.
1175 **C** The same as panel B but for DAPI and msfGFP.
1176 **D** Representative images of DAPI-stained CJW5685 cells expressing RNase E ΔMTS
1177 labeled with mCherry in exponential (OD 0.1) and transition phases (OD 1.30) along with
1178 signal intensity profiles for the indicated (*) cell. Scale bar: 2 μm
1179 **E** Distributions of SCF values between DAPI and RNase E ΔMTS-mCherry for
1180 exponential (n = 281 cells) and transition (n = 3174 cells) phases.
1181
1182 **Fig 3: Subcellular rearrangement of the cytoplasm is not driven by inner membrane**
1183 **collapse or nucleoid association.**
1184 **A** Images of MitoTracker Green-labeled cells (CJW7324) in exponential and transition
1185 phase. Fluorescence intensities are indicated in arbitrary units (a.u.). Signal intensity
1186 profiles are provided for the cells indicated by asterisks. White arrows indicate signal
1187 depletion at a pole. Scale bar: 2 μm

1188 **B** Timelapse sequence of a cell (CJW5159) expressing RplA-GFP and HupA-mCherry,
1189 with N and O indicating the new and old poles, respectively. Cells in late exponential
1190 phase (OD ~0.5) were washed in spent medium from a transition-phase culture (OD =
1191 2.63) and spotted on an agarose pad containing the same spent medium. The RplA-GFP
1192 images were scaled to reflect the 5-95% range of signal intensity for each image. Next to
1193 the image series is the signal intensity profile for the cell indicated by an asterisk. Scale
1194 bar: 2 μm
1195 **C** Representative phase contrast and fluorescence images of cephalexin-treated and
1196 DAPI-labeled CJW7325 cells carrying RplA-mCherry and msfGFP in transition phase,
1197 with the corresponding signal intensity profiles. Fluorescence intensities are indicated in
1198 arbitrary units (a.u.). Scale bar: 5 μm
1199 **D** Same as C but showing a band of enriched msfGFP signal (purple arrowhead) in the
1200 region lacking DAPI staining (grey bracket). Scale bar: 5 μm
1201 **E** Phase contrast and fluorescence images of a CJW7326 cell carrying HupA-mCherry
1202 and msfGFP, with the corresponding signal intensity profile. Scale bar: 1 μm
1203
1204 **Fig 4: Glycogen accumulation in transition phase drives cellular rearrangement.**
1205 **A** Representative relative whole cell ^{13}C CPMAS spectral overlays of WT cell extracts
1206 (strain CJW2168) from cultures in exponential vs. transition phase (top), purified bovine
1207 and mussel glycogen (middle), and WT vs. Δ*glgBXCAP* (CJW7537) cell extracts from
1208 transition phase cultures (bottom). Dashed rectangle indicates sugar carbon region of
1209 spectrum.

1210 **B** Representative images of WT (CJW7606) and Δ*glgBXCAP* (CJW7607) cells in
1211 transition phase (OD 2.7) labeled with DAPI and expressing mScarlet and the glycogen
1212 sensor, along with the signal intensity profiles for indicated (*) cells. Fluorescence
1213 intensities are indicated in arbitrary units (a.u.). Scale bar: 2 μm
1214 **C** Distributions of SCF values of the glycogen sensor vs. DAPI or mScarlet for WT cells
1215 (n = 3591) in transition phase.
1216 **D** Density contour plot showing the area difference of glycogen sensor signal between
1217 the cell poles normalized by the cell area versus the nucleoid asymmetry (n = 5794 cells).
1218 The latter was calculated by determining the offset of the nucleoid mid-point from cell
1219 center normalized to cell length. The contour lines represent the 0.10, 0.2, 0.3, 0.4, 0.50,
1220 0.6, 0.7, 0.8 and 0.9 probability envelopes of the data. Spearman correlation coefficient
1221 (ρ) is 0.748 (p-value = 0).
1222 **E** Example phase contrast and fluorescence images of DAPI-labeled CJW7606 cell
1223 carrying mScarlet and the glycogen sensor. The cell was from a culture in transition phase
1224 following cephalexin treatment. Grey bracket indicates DNA-free region where glycogen
1225 accumulation (orange arrowheads) sandwiches a band of RplA-mCherry enrichment
1226 (purple arrowhead). To the right is the corresponding signal intensity profile, where the
1227 grey shading indicates the DNA free-region with bands of glycogen biosensor and RplA-
1228 mCherry enrichment. Scale bar: 2 μm
1229
1230
1231

1232 **Fig 5. Mimicking intracellular conditions of crowding and ionic strength induces**
1233 **phase transition of glycogen into liquid condensates that partially exclude GFP.**
1234 **A** Plot showing dynamic light scattering (DLS) measurements of the particle diameter size
1235 for PEG and PEO polymers of different molecular weights in IS buffer. Samples were
1236 measured in triplicate for 300 s at 25°C with a 90-degree detection angle. The line
1237 indicates the empirical relation (hydrodynamic diameter ($\sigma_{PEG/PEO}$) =
1238 $0.029*MW_{PEG/PEO}^{(0.571\pm0.009)}$) determined by Devanand and Selser (1991).
1239 **B** Phase contrast and ConA-FITC fluorescence images of representative fields of view
1240 showing no LLPS (left), LLPS (center), and collapsed aggregates (right) obtained with the
1241 indicated concentrations of 3 kDa PEG. All samples were made using the IS buffer and
1242 contained 9 g/L of glycogen. Scale bar: 10 μm
1243 **C** Example montages of glycogen condensates labeled with ConA-FITC undergoing
1244 fusion events over time. Scale bar: 3 μm
1245 **D** Fluorescence images of ConA-FITC-labeled glycogen condensates imaged at t ~ 3 min
1246 and t ~ 30 min after the addition of 3 kDa PEG. Scale bar: 10 μm
1247 **E** Phase diagram of glycogen phases as a function of glycogen and 3 kDa PEG
1248 concentrations.
1249 **F** Plot showing the minimal concentration required to drive LLPS as a function of the
1250 average Stokes diameters for all tested PEG/PEO crowders. Phase separation was
1251 determined by assessing the formation of droplets using phase contrast imaging. The
1252 average diameter for each PEG/PEO crowder corresponds to the measurements shown
1253 in (A).

1254 **G** Phase contrast images of representative fields of view of glycogen (10 g/L) in IS buffer
1255 mixed with the indicated concentration and molecular weight of PEG or PEO (separately
1256 or combined). Scale bar: 10 μm
1257 **H** Phase contrast images of glycogen (10 g/L) and 3 kDa PEG (20 mM) mixtures in IS
1258 buffer before and after a two-fold dilution. For both conditions, imaging was performed
1259 within 1 min after mixing. Scale bar: 10 μm
1260 **I** Phase contrast and GFP images of a representative field of view of glycogen (10g/L) in
1261 IS buffer mixed with GFP (15 μM) and 3 kDa PEG (20 mM). Scale bar: 10 μm
1262
1263 **Fig 6: Asymmetry in glycogen accumulation creates cell size differences and**
1264 **asymmetric cell divisions.**
1265 **A** Example images of an asymmetrically dividing cell (CJW7606) in transition phase. The
1266 cell expresses the glycogen sensor and mScarlet. Fluorescence intensities are indicated
1267 in arbitrary units (a.u.). Scale bar: 2 μm
1268 **B** Scatter plot of the difference in cell area and the difference in the area occupied by the
1269 glycogen sensor between future daughter cells. Constricting cells (n = 365) were divided
1270 into two future daughter cells based on the cell constriction position (illustrated in the
1271 inset). Spearman correlation coefficient (ρ) is 0.54 (p-value = 1.28×10^{-27}).
1272 **C** Schematic of co-cultured pairs of WT and Δ*glgBXCAP* cells constitutively expressing
1273 mSCFP3 or mVenus.
1274 **D** Plot showing the percentage difference in area between co-cultured WT and
1275 Δ*glgBXCAP* cells carrying either mVenus (yellow) or mSCFP3 (cyan). The names of the
1276 co-cultured strain pairs are Mix 1 (CJW7666/CJW7667) and Mix 2 (CJW7665/CJW7668).

1277 Each marker (black diamond) corresponds to the average percent difference in cell area
1278 (100%*((WT-Δ*glgBXCAP)* /Δ*glgBXCAP*)) for each co-culture biological replicate. It
1279 corresponds to the mean of the distribution of the cell area difference statistics generated
1280 using bootstrapping for each biological replicate (n = 500 samplings). Error bars
1281 correspond to the standard deviations of the combined distributions of size differences
1282 across all biological replicates.
1283 **E** Density contour plots of the relative division position as a function of the nucleoid
1284 centroid position in dividing cells for transition-phase cells (n > 123) from co-cultured pairs
1285 shown in panel D. The values +0.5 and -0.5 represent cell poles while 0 corresponds to
1286 the cell center. Spearman correlation coefficient (ρ) for WT cells is 0.893 (p-value = 0) for
1287 mix 1 and 0.836 (p-value = 0) for mix 2.

1288 **TABLES**

1289 **Table 1. Calculated concentrations of glycogen and proteins in *E. coli* in different**

1290 **growth conditions.**

Glycogen			
Reported (mg/g dry weight)	Conversion (g/L)	Conditions	References
13	1.43	Exponential phase, 1% glucose in enriched medium (with yeast extract) at 37°C	(Govons *et al*, 1969; Preiss & Romeo, 1994)
2.5	8.25	Exponential phase, glucose minimal media at 37°C, 40 min division rate	(Ingraham *et al*, 1983)
2.8-4.4	9.24-14.52	Stationary phase, LB at 37°C	(Wang *et al*, 2019a)
19	20.9	Stationary phase, 1% glucose in enriched medium (with yeast extract) at 37°C	(Preiss & Romeo, 1994; Govons *et al*, 1969)
Proteins			
Reported	Conversion (mM)	Conditions	References
2.35×10^6 proteins per cell	4.48	Exponential phase, glucose minimal medium at 37°C, 40 min division rate	(Neidhardt & Curtiss, 1996)
0.24 g/mL	9.6-12	Calculated for proteins between 20 and 25 kDa	(Ingraham *et al*, 1983)

1291

1292 Glycogen and protein concentrations used in our study were taken from reported values

1293 for *E. coli* cells growing in different conditions. Glycogen concentrations from dry weight

1294 measurements (mg/g cells) were converted to wet weight values using a water content

1295 value of 70% (Bremer & Dennis, 2008; Feijó Delgado *et al*, 2013). To obtain the

1296 concentrations in g/L, we used a cell density of 1.1 g/mL (Kubitschek *et al*, 1983;

1297 Loferer-Krössbacher *et al*, 1998). To calculate the protein concentrations in mM from

1298 proteins per cell, we used a cell volume of 0.86 μm^3 (Kubitschek & Friske, 1986; Milo,

1299 2013). To obtain the mM concentrations from g/mL, we used the indicated molecular

1300 weight range.

1301

1302 **Table 2. Calculated concentrations of ribosomes and polysomes used in this**

1303 **study.**

Ribosomes per cell	Conditions	Cell volume (μm^3)	Estimated ribosome concentration (μM)	Estimated polysome concentration (μM)	References
3500	Stationary phase, LB at 37°C	1	5.8	1.16	(Nilsson *et al*, 1997)
15000	Exponential phase, M9Gly at 37°C, 60 min doubling time	1	24.9	4.98	(Bremer & Dennis, 2008)
61000	Exponential phase, M9GluCAA at 37°C, 24 min doubling time	3.5	28.9	5.79	(Bremer & Dennis, 2008)

1304

1305 Concentrations were determined from the reported numbers of ribosomes per cell using

1306 the Avogadro constant to calculate number of moles per cell, then dividing by the reported

1307 cell volume values indicated (Floc'h *et al*, 2019; Kubitschek & Friske, 1986). For

1308 polysomes, an active fraction of 0.8 percent was used (Bremer & Dennis, 2008) and a

1309 polysome was assumed to consist of four ribosomes (Brandt *et al*, 2009).

1310

1311

1312 **Table 3. Conditions that resulted in fluorescent protein (FP) exclusion from**

1313 **glycogen LLPS in vitro.**

PEG/PEO (MW)	PEG/PEO concentration	Temperature (°C)	FP	Buffer	FP exclusion
1.5 kDa	60 mM	30	GFP	IS	Yes
3 kDa	20 mM	25	GFP	IS	Yes
3 kDa	20 mM	30	GFP	IS	Yes
3 kDa	20 mM	37	GFP	IS	Yes
3 kDa	20 mM	25	GFP	IS without $MgCl_2$	Yes
3 kDa	20 mM	25	mCherry	IS	Yes
4 kDa	15 mM	25	GFP	IS	Yes
4 kDa	15 mM	30	GFP	IS	Yes
4 kDa	15 mM	37	GFP	IS	Yes
8 kDa	3 mM	25	GFP	IS	Yes
8 kDa	3 mM	30	GFP	IS	Yes
20 kDa	750 μM	30	GFP	IS	Yes
100 kDa	20 μM	25	GFP	IS	Yes
1 MDa	10 μM	25	GFP	IS	Yes

1314

1315 Summary of the assays performed for testing the exclusion of FPs by glycogen liquid

1316 condensates. FP exclusion was detected by phase contrast and fluorescence imaging.

1317 For all assays, 10 g/L of glycogen and 15 μM of the FP (GFP or mCherry) were used.

1318 **Table 4: Strains used in this study.**

Identifier	Genotype	Source or construction method
MG1655	F-lambda- *ilvG- rfb-*50 *rph*-1	(Jensen, 1993)
CJW4677	MG1655 *rplA*::*rplA-gfp*	(Gray *et al*, 2019)
CJW5685	MG1655 *rne*::*rneΔMTS-mCherry*	From Dr. Sangjin Kim
CJW7006	MG1655/pEB2-mScarlet-I	Gift from Philippe Cluzel; AddGene plasmid #104007. (Balleza *et al*, 2018)
CJW7020	MG1655 *rplA*::*rplA-msfGFP*	(Gray *et al*, 2019)
CJW7021	MG1655 *rpsB*::*rpsB-msfGFP*	(Gray *et al*, 2019)
CJW7083	MG1655 *attB*::P_{proC}-*msfGFP*-FRT-*kan*-FRT	pKD13 was amplified from plasmid pKD13-msfGFP (Gray *et al*, 2019) using primers YP32 and YP33, with YP32 encoding a transcriptional terminator sequence. *msfGFP* was also amplified from this plasmid using YP34 and YP35. Constitutive synthetic promoter P_{proC} was amplified from CJW7006 using primers YP36 and YP37, with YP37 also encoding the ribosome binding site L3S1P13 (Chen *et al*, 2013), linker sequence and start codon. These pieces were assembled using Gibson assembly. The construct was then integrated into the chromosome of MG1655 at the *attB* site using lambda red recombination.
CJW7275	MG1655 *attB*::P_{proC}-*msfGFP*	The kanamycin resistance cassette of CJW7083 was excised by transiently equipping this strain with plasmid pCP20, expressing the Flp site specific recombinase (Cherepanov & Wackernagel, 1995).
CJW7324	MG1655 *rplA*::*rplA-mCherry*	(Gray *et al*, 2019)
CJW7325	MG1655 *rplA*::*rplA-mCherry attB*::P_{proC}-*msfGFP*	*attB*::PproC-msfGFP - KAN from CJW7083 was moved into CJW7324 by P1 transduction. Colonies were screened for kanamycin resistance and GFP fluorescence. The kanamycin resistance cassette was excised by transiently

		equipping this strain with plasmid pCP20, expressing the Flp site specific recombinase (Cherepanov & Wackernagel, 1995).
CJW7326	MG1655 *attB*::P_{proC}-*msfGFP hupA*::*hupA-mCherry*	*hupA-mCherry*-FRT-*kan*-FRT from CJW5158 (Gray *et al*, 2019) was moved into CJW7275 by P1 transduction. Colonies were screened for kanamycin resistance and mCherry fluorescence. The kanamycin resistance cassette was excised by transiently equipping this strain with plasmid pCP20, expressing the Flp site specific recombinase (Cherepanov & Wackernagel, 1995).
CJW7485	MG1655 *rplA*::*rplA-mCherry*/pBAD-GFP(-30)	CJW7324 was transformed with plasmid pBAD-GFP(-30).
CJW7486	MG1655 *rplA*::*rplA-mCherry*/pBAD-GFP(-7)	CJW7324 was transformed with plasmid pBAD-GFP(-7).
CJW7487	MG1655 *rplA*::*rplA-mCherry*/pBAD-GFP(0)	CJW7324 was transformed with plasmid pBAD-GFP(0).
CJW7488	MG1655 *rplA*::*rplA-mCherry*/pBAD-GFP(+7)	CJW7324 was transformed with plasmid pBAD-GFP(+7).
CJW7489	MG1655 *rplA*::*rplA-mCherry*/pBAD-GFP(+11a)	CJW7324 was transformed with plasmid pBAD-GFP(+11a).
CJW7490	MG1655 *rplA*::*rplA-mCherry*/pBAD-GFP(+11b)	CJW7324 was transformed with plasmid pBAD-GFP(+11b).
CJW7491	MG1655 *rplA*::*rplA-mCherry*/pBAD-GFP(+15)	CJW7324 was transformed with plasmid pBAD-GFP(+15).
CJW7492	MG1655 *rplA*::*rplA-mCherry*/pBAD-GFP(+25)	CJW7324 was transformed with plasmid pBAD-GFP(+25).
CJW7537	MG1655 Δ*glgBXCAP*-FRT-*kan*-FRT	The glycogen operon was replaced with a kanamycin cassette using lambda red from the plasmid pSIM6 (Diner *et al*, 2011) using gene block gb_1. Candidate colonies we confirmed by PCR.

CJW7587	MG1655 Δ*glgBXCAP*	The kanamycin resistance cassette from CJW7537 was excised by transiently equipping this strain with plasmid pCP20, expressing the Flp site specific recombinase (Cherepanov & Wackernagel, 1995).
CJW7588	MG1655 *lacY(A177C) araFGH*::*spec* Δ*lacI* Δ*araE araBAD*::*dCas9 galM* <*PBBa-J23119-sgRNA(ftsZ)-(S. pyogenes* terminator*)-(rrnB* terminator*)*> *gmpA attB*::P_{proC}-*msfGFP*	*attB*::P_{proC}-*msfGFP*-FRT-*kan*- FRT from CJW7083 was moved into SJ_XTL229 by P1 transduction. Colonies were screened for kanamycin resistance and GFP fluorescence. The kanamycin resistance cassette was excised by transiently equipping this strain with plasmid pCP20, expressing the Flp site specific recombinase (Cherepanov & Wackernagel, 1995).
CJW7601	MG1655 Tn7::P_{tac}-*GFPmut3-CBM20* FRT-*cat*-FRT	Plasmid pNDL-1-P_{tac}-GFPmut3-CBM20 FRT-CmR-FRT was transformed into MG1655. Colonies were screened for ampicillin resistance at 30°C. Integration was then carried out by incubating at 37°C and selecting for chloramphenicol resistance
CJW7604	MG1655 *ΔglgBXCAP* Tn7::P_{tac}-*GFPmut3-CBM20*-FRT-*cat*-FRT	Plasmid pNDL-1-P_{tac} -GFPmut3-CBM20 FRT-CmR-FRT was transformed into CJW7587. Colonies were screened for ampicillin resistance at 30°C. Integration was then carried out by incubating at 37°C and selecting for chloramphenicol resistance
CJW7606	MG1655 Tn7:: P_{tac} -*GFPmut3-CBM20*-FRT-*cat*-FRT	CJW7601 was transformed with pEB2-mScarlet-I.
CJW7607	MG1655 Δ*glgBXCAP* Tn7::P_{tac}-*GFPmut3-CBM20* FRT-*cat* -FRT	CJW7604 was transformed with pEB2-mScarlet-I.
CJW7660	MG1655 *hupA*::*hupA-mCherry*	*hupA-mCherry*-FRT-*kan*-FRT from CJW5158 (Gray *et al*, 2019) was moved into MG1655 by P1 transduction. Colonies were screened for kanamycin resistance and mCherry fluorescence. The kanamycin resistance cassette was excised by transiently equipping this strain with plasmid pCP20, expressing the Flp site specific recombinase (Cherepanov & Wackernagel, 1995).

CJW7661	MG1655 Δ*glgBXCAP hupA*::*hupA-mCherry*	*hupA-mCherry*-FRT-*kan*-FRT from CJW5158 (Gray *et al*, 2019) was moved into CJW7587 by P1 transduction. Colonies were screened for kanamycin resistance and mCherry fluorescence. The kanamycin resistance cassette was excised by transiently equipping this strain with plasmid pCP20, expressing the Flp site specific recombinase (Cherepanov & Wackernagel, 1995).
CJW7665	MG1655 *hupA*::*hupA-mCherry* Tn7:: P_{RpsL}-*mSCFP3*-FRT-*kan*-FRT	Tn7:: P_{RpsL}-*mSCFP3*-FRT-*kan*-FRT from JP1456 was moved into CJW7660 by P1 transduction. Colonies were screened for kanamycin resistance and CFP fluorescence.
CJW7666	MG1655 *hupA*::*hupA-mCherry* Tn7:: P_{RpsL}-*mVenus*-FRT-*kan*-FRT	Tn7:: P_{RpsL}-*mVenus*-FRT-*kan*- FRT from JP1457 was moved into CJW7660 by P1 transduction. Colonies were screened for kanamycin resistance and YFP fluorescence.
CJW7667	MG1655 Δ*glgBXCAP hupA*::*hupA-mCherry* Tn7:: P_{Rps}-*mSCFP3*-FRT-*kan*-FRT	Tn7:: P_{Rps}-*mSCFP3*-FRT-*kan*-FRT from JP1456 was moved into CJW7661 by P1 transduction. Colonies were screened for kanamycin resistance and CFP fluorescence.
CJW7668	MG1655 Δ*glgBXCAP hupA*::*hupA-mCherry* Tn7:: P_{Rps}-*mVenus*-FRT-*kan*-FRT	Tn7::P_{Rps}-*mVenus*-FRT-*kan*- FRT from JP1457 was moved into CJW7661 by P1 transduction. Colonies were screened for kanamycin resistance and YFP fluorescence.
CJW7718	MG1655 Δ*glgBXCAP* /pEB2-mScarlet-I	CJW7587 was transformed with plasmid pEB2-mScarlet-I.
JP1456	MG1655 *Tn7*:: P_{Rps}*L*-*mSCFP3*-FRT-*kan*-FRT	Gift from Johan Paulsson
JP1457	MG1655 *Tn7*::P_{RpsL}-*mVenus*-FRT-*kan*-FRT	Gift from Johan Paulsson
SJ_XTL229	MG1655 *lacY(A177C) araFGH*::*spec* Δ*lacI* Δ*araE araBAD*::*dCas9 galM* <*PBBa-J23119-sgRNA(ftsZ)-(S. pyogenes* terminator*)-(rrnB* terminator*)*> *gmpA*	(Li *et al*, 2016)

1319

1320 **Table 5. Plasmids used in this study.**

Identifier	Source or description method
pBAD-GFP (-30)	(Schavemaker *et al*, 2017)
pBAD-GFP (-7)	(Schavemaker *et al*, 2017)
pBAD-GFP (0)	(Schavemaker *et al*, 2017)
pBAD-GFP (+7)	(Schavemaker *et al*, 2017)
pBAD-GFP (+11a)	(Schavemaker *et al*, 2017)
pBAD-GFP (+11b)	(Schavemaker *et al*, 2017)
pBAD-GFP (+15)	(Schavemaker *et al*, 2017)
pBAD-GFP (+25)	(Schavemaker *et al*, 2017)
pEB2-mScarlet-I	Gift from Philippe Cluzel; AddGene plasmid #104007 (Balleza *et al*, 2018)
pkD13-msfGFP	(Gray *et al*, 2019)
pNDL-1-P_{tac}-GFPmut3-CBM20 FRT-CmR-FRT	Gene block gb_2 was integrated into the pNDL-1 plasmid using BP clonase and colonies were isolated using counter selection for the CcdB toxin (Landgraf *et al*, 2012).

1321

1322

1323 **Table 6. Oligos used in this study.**

Identifier	Sequence (5’ to 3’)
gb_1	TCAATAATACCGGCAAGTCCGACACCCAGCATGGCAATAACCACCGCCAAA AATTGCGCCAGTATGGGGATGCCGAAAAAAGTCATTACCAGCGAGGTCAAA ATCCATTTTCTGTTTTGCATTATTCTTTCCATTCTTTTTGAATGGTGAAATTAT ACTCCCCGAGTCCCCTTGCCCCTTCTGGACACTTTTCCGAAATGATGGCGG AAAAAAACGGGACCCTTTGGCCCCGTTCTATTTATTGGTGAACGTGTAGGC TGGAGCTGCTTCGAAGTTCCTATACTTTCTAGAGAATAGGAACTTCGGAATA GGAACTTCAAGATCCCCTTATTAGAAGAACTCGTCAAGAAGGCGATAGAAG GCGATGCGCTGCGAATCGGGAGCGGCGATACCGTAAAGCACGAGGAAGC GGTCAGCCCATTCGCCGCCAAGCTCTTCAGCAATATCACGGGTAGCCAAC GCTATGTCCTGATAGCGGTCCGCCACACCCAGCCGGCCACAGTCGATGAA TCCAGAAAAGCGGCCATTTTCCACCATGATATTCGGCAAGCAGGCATCGCC ATGGGTCACGACGAGATCCTCGCCGTCGGGCATGCGCGCCTTGAGCCTG GCGAACAGTTCGGCTGGCGCGAGCCCCTGATGCTCTTCGTCCAGATCATC CTGATCGACAAGACCGGCTTCCATCCGAGTACGTGCTCGCTCGATGCGAT GTTTCGCTTGGTGGTCGAATGGGCAGGTAGCCGGATCAAGCGTATGCAGC CGCCGCATTGCATCAGCCATGATGGATACTTTCTCGGCAGGAGCAAGGTG AGATGACAGGAGATCCTGCCCCGGCACTTCGCCCAATAGCAGCCAGTCCC TTCCCGCTTCAGTGACAACGTCGAGCACAGCTGCGCAAGGAACGCCCGTC GTGGCCAGCCACGATAGCCGCGCTGCCTCGTCCTGCAGTTCATTCAGGGC ACCGGACAGGTCGGTCTTGACAAAAAGAACCGGGCGCCCCTGCGCTGACA GCCGGAACACGGCGGCATCAGAGCAGCCGATTGTCTGTTGTGCCCAGTCA TAGCCGAATAGCCTCTCCACCCAAGCGGCCGGAGAACCTGCGTGCAATCC ATCTTGTTCAATCATGCGAAACGATCCTCATCCTGTCTCTTGATCAGATCTT GATCCCCTGCGCCATCAGATCCTTGGCGGCAAGAAAGCCATCCAGTTTACT TTGCAGGGCTTCCCAACCTTACCAGAGGGCGCCCCAGCTGGCAATTCCGG TTCGCTTGCTGTCCATAAAACCGCCCAGTCTAGCTATCGCCATGTAAGCCC ACTGCAAGCTACCTGCTTTCTCTTTGCGCTTGCGTTTTCCCTTGTCCAGATA GCCCAGTAGCTGACATTCATCCGGGGTCAGCACCGTTTCTGCGGACTGGC TTTCTACGTGTTCCGCTTCCTTTAGCAGCCCTTGCGCCCTGAGTGCTTGCG GCAGCGTGAGCTTCAAAAGCGCTCTGAAGTTCCTATACTTTCTAGAGAATA GGAACTTCGGCTTGTCTTCCTGTTTTATTGTGTCACCCCATCCAATTGGATT TTTGACTTCTGGTTGTGACATTTTTTTGACCTGAACGGCGCAGCACTCTGTG CATCCTCTCTGCGTCGTCCTCACTTCAGGTAAGGCTGTGAATACTCATGTA TTCAGCCACCCTTAAAGAATAGCCAATGCTCTATTTAACTCCCGGTAAATCA TGAAACATCTGCGCTTACTCCTGTATTACGCACTAACAGGGGCGGCATCGC GCCCCAGATTTAATGAATAAAGATTACGCCAGTT
gb_2	CACCGAATTCCCCGGGGGGGACAAGTTTGTACAAAAAAGCAGGCTTACGA CATCATAACGGTTCTGGCAAATATTCTGAAATGAGCTGTTGACAATTAATCA TCGGCTCGTATAATGTGTGGAATTGTGAGCGGATAACAATTTCACACAGGA AACAGAATATGAGTAAAGGAGAAGAACTTTTCACTGGAGTTGTCCCAATTCT TGTTGAATTAGATGGTGATGTTAATGGGCACAAATTTTCTGTCAGTGGAGA GGGTGAAGGTGATGCAACATACGGAAAACTTACCCTTAAATTTATTTGCACT ACTGGAAAACTACCTGTTCCATGGCCAACACTTGTCACTACTTTCGGTTATG

	GTGTTCAATGCTTTGCGAGATACCCAGATCATATGAAACAGCATGACTTTTT CAAGAGTGCCATGCCCGAAGGTTATGTACAGGAAAGAACTATATTTTTCAA AGATGACGGGAACTACAAGACACGTGCTGAAGTCAAGTTTGAAGGTGATAC CCTTGTTAATAGAATCGAGTTAAAAGGTATTGATTTTAAAGAAGATGGAAAC ATTCTTGGACACAAATTGGAATACAACTATAACTCACACAATGTATACATCA TGGCAGACAAACAAAAGAATGGAATCAAAGTTAACTTCAAAATTAGACACAA CATTGAAGATGGAAGCGTTCAACTAGCAGACCATTATCAACAAAATACTCCA ATTGGCGATGGCCCTGTCCTTTTACCAGACAACCATTACCTGTCCACACAA TCTAAGCTTTCGAAAGATCCCAACGAAAAGAGAGACCACATGGTCCTTCTT GAGTTTGTAACAGCTGCTGGGATTACACATGGCATGGATGAACTATACAAA AGCGATTTCATGCCTGCCGGTTCTCAACAGGTTAGCGTTCGTTTTCAGGTA CACTACGTCACTTCCACCGACGTTCAGTTTATTGCAGTGACCGGCGATCAC GAGTGCCTGGGCCGCTGGAACACGTACATCCCTCTGCACTACAACAAAGA CGGTTTCTGGTCCCACAGCATCTTTCTGCCGGCGGATACCGTTGTGGAGT GGAAATTTGTTCTGGTTGAAAACGGTGGCGTTACGCGTTGGGAGGAATGTT CCAACCGTTTCCTGGAAACCGGTCACGAAGATAAGGTAGTTCACGCGTGG TGGGGTATCCATTAAATGTCCAGACCTGCAGGCATGCAAGCTCTAGTTGGA TTCTCACCAATAAAAAACGCCCGGCGGCAACCGAGCGTTCTGAACAAATCC AGATGGAGTTCTGAGGTCATTACTGGATCTATCAACAGGAGTCCAAGCGAG CGAATTCTGCAGGTGTTAATTCAGGAGCATTGTTATCAGACCAAATATGTGT AGGCTGGAGCTGCTTCGAAGTTCCTATACTTTCTAGAGAATAGGAACTTCG GAATAGGAACTTCTTATCAAAAAGGATCTTCACCTAGATCCTTTTAAATTAAA AATGAAGTTTTAAATCAATCTAAAGTATATATGAGTAAACTTGGTCTGACAG CTCGAGGCGCTCGATATCAAATTACGCCCCGCCCTGCCACTCATCGCAGT ACTGTTGTAATTCATTAAGCATTCTGCCGACATGGAAGCCATCACAAACGG CATGATGAACCTGAATCGCCAGCGGCATCAGCACCTTGTCGCCTTGCGTAT AATATTTGCCCATGGTGAAAACGGGGGCGAAGAAGTTGTCCATATTGGCCA CGTTTAAATCAAAACTGGTGAAACTCACCCAGGGATTGGCTGAGACGAAAA ACATATTCTCAATAAACCCTTTAGGGAAATAGGCCAGGTTTTCACCGTAACA CGCCACATCTTGCGAATATATGTGTAGAAACTGCCGGAAATCGTCGTGGTA TTCACTCCAGAGCGATGAAAACGTTTCAGTTTGCTCATGGAAAACGGTGTA ACAAGGGTGAACACTATCCCATATCACCAGCTCACCGTCTTTCATTGCCAT ACGAAATTCCGGATGAGCATTCATCAGGCGGGCAAGAATGTGAATAAAGG CCGGATAAAACTTGTGCTTATTTTTCTTTACGGTCTTTAAAAAGGCCGTAAT ATCCAGCTGAACGGTCTGGTTATAGGTACATTGAGCAACTGACTGAAATGC CTCAAAATGTTCTTTACGATGCCATTGGGATATATCAACGGTGGTATATCCA GTGATTTTTTTCTCCATTTTAGCTTCCTTAGCTCCTGAAAATCTCGATAACTC AAAAAATACGCCCGGTAGTGATCTTATTTCATTATGGTGAAAGTTGGAACCT CTTACGTGCCCGATCAACTCGAGTGCCACCTGACGTCTAAGAAACCATTAT TATCATGACATTAACCTATAAAAATAGGCGTATCACGAGGCAGAATTTCAGA TAAAAAAAATCCTTAGCTTTCGCTAAGGATGATTTCTGGAAGCGCTCTGAAG TTCCTATACTTTCTAGAGAATAGGAACTTCGTACCCAGCTTTCTTGTACAAA GTGGTCCCCAAGCTTCTGCAGAGCT
YP32	TACTAGAGGACGAACAATAAGGCCTCCCTAACGGGGGGCCTTTTTTATTGA TAACAAAAGTGTAGGCTGGAGCTGCTTCG
YP33	AATCGCTCAAGACGTGTAATGCTGCAATC

YP34	TCAAAAGGCGAAGAACTTTTTACCG
YP35	TAGGGAGGCCTTATTGTTCGTCCTCTAGTATTATTTATACAATTCATCCATTCCATGAGTGA
YP36	CCAGTGCCAAGCTTGCATGCAGATTGCAGCATTACACGTCTTGAGCGATTCACAGCTAACACCACGTCG
YP37	TACACCGGTAAAAAGTTCTTCGCCTTTTGACATCTAGTATTCTCCTCTTTCTCTAGTAAAAGTTAAACAAAATTATTTGTAGAGGGAAAC

1326 **EXPANDED VIEW FIGURE LEGENDS**

1327 **Fig EV1: Example images of cells in different growth phases.**

1328 Shown are overlays of two representative phase contrast and fluorescence images of
1329 DAPI-stained *E. coli* cells (CJW4677) in exponential (OD 0.34), transition (OD 2.35), and
1330 stationary phase (OD 3.24). Scale bar: 5 µm

1331

1332 **Fig EV2: Consistency of cytoplasmic probe localization in transition phase.**

1333 **A** Representative fluorescence images of DAPI-stained *E. coli* cells expressing different
1334 ribosomal protein fusions in transition phase: RplA-GFP (CJW4677), RplA-msfGFP
1335 (CJW7020), and RpsB-msfGFP (CJW7021). Arrowheads indicate cell areas of ribosome
1336 depletion. Scale bar: 2 µm

1337 **B** Representative fluorescence image of DAPI-stained *E. coli* cells (CJW7006) expressing
1338 mScarlet in transition phase. Arrowheads indicate cell areas of mScarlet depletion. Scale
1339 bar: 2 µm

1340 **C** Representative fluorescence images of DAPI-stained *E. coli* expressing RplA-mCherry
1341 as well as free fluorescent GFP variants with different net surface charges: -30
1342 (CJW7485), -7 (CJW7486), 0 (CJW7487), +7 (CJW7488), +11a (CJW7489), +11b
1343 (CJW7490), +15 (CJW7491), and +25 (CJW7492). For GFP with a net surface charge
1344 +11, 'a' and 'b' refer to variations in distribution of the charge on the protein surface
1345 (Schavemaker *et al*, 2017). Cells were grown in M9GluCAAT and supplemented with
1346 0.4% arabinose to induce GFP expression. Arrowheads indicate cell areas depleted of
1347 GFP. Scale bar: 2 µm

1348 **D** Fluorescence images of representative DAPI- and RNASelect-labeled *E. coli* cells
1349 (CJW7324) in exponential (OD 0.30) and transition (OD 1.72) phase. Also shown are the
1350 corresponding fluorescence signal profiles for the indicated (*) cells. Arrowheads indicate
1351 areas depleted of RNASelect. Scale bar: 2 μm
1352 **E)** Distributions of SCF values between DAPI and RNASelect for exponential (n = 507
1353 cells) and transition (n = 1492 cells) phases.
1354
1355 **Fig EV3: Colocalization of nucleoid and protein probe in FtsZ-depleted cells in**
1356 **transition phase.**
1357 Sample images of DAPI-stained FtsZ-depleted cells expressing cytoplasmic msfGFP
1358 (CJW7588) in transition phase in M9GluCAAT supplemented with 0.4% arabinose to
1359 induce the CRISPRi system, thereby blocking the expression of *ftsZ*. The corresponding
1360 signal intensity profile is shown below. Scale bar: 5 μm
1361
1362 **Fig EV4: Localization of the fluorescent glucose analog 2-NBDG relative to that of**
1363 **ribosomes during transition phase.**
1364 Image of a cephalexin-treated cell (CJW7324) expressing RplA-mCherry in transition
1365 phase. Cells were grown in M9CAAT supplemented with 0.2% L-arabinose. Cells were
1366 incubated with 2-NBDG and DAPI for 10 min and washed twice in spent medium prior to
1367 imaging. Yellow arrowheads indicate accumulations of 2-NBDG that sandwich an
1368 accumulation of RplA-mCherry signal. Below is the cell signal intensity profile, with the
1369 grey shade highlighting the region of interest. Scale bar: 5 μm
1370

1371 **Fig EV5: Replicates of co-culture experiments.**

1372 Quantification of relative nucleoid centroid position and division position in dividing cells
1373 (constriction > 0.1) for transition phase cells in co-cultured pairs of panel D. +0.5 and 0.5
1374 represent cell poles while 0 is cell center. n > 150 cells.

1375

1376 **EXPANDED VIEW VIDEO LEGENDS**

1377 **Video EV1: Timelapse sequence showing that nucleoids and ribosomes remain**
1378 **closer to the new pole upon division during transition phase.**

1379 Montage video showing phase and fluorescence overlays of a representative cell
1380 expressing RplA-msGFP and HupA-mCherry (CJW5159) growing and dividing in
1381 transition phase. Cells from a culture in late exponential phase (OD = 0.5) were washed
1382 in transition phase medium, spotted on an agarose pad containing transition phase
1383 medium (OD = 2.63), and imaged every 2 min. Time stamp shows h:min:s.

1384

1385 **Video EV2: Timelapse sequence showing glycogen condensate fusions.**

1386 Timelapse sequence of glycogen LLPS droplets labeled with ConA-FITC as they fuse. A
1387 LLPS sample was made with 10 g/L of glycogen and 20 mM of 3 kDa PEG in IS buffer.
1388 Phase contrast (left) and FITC (right) images were acquired every 10 s at 25°C. Time
1389 stamp shows h:min:s.

1390

1391 **Video EV3: Timelapse sequence of "collapsed" glycogen aggregates.**

1392 Timelapse sequence showing the "collapsed" phase-separated glycogen undergoing
1393 collisions that do not result in fusion events. The sample was made with 10 g/L of

1394 glycogen and 30 mM of 3kDa PEG in the IS buffer. Phase contrast images were acquired
1395 every 10 s at 25°C. Time stamp shows h:min:s.
1396
1397 **Video EV4: Z-stack sequence of glycogen condensates excluding GFP.** Z-stacks of
1398 both phase contrast and GFP of glycogen LLPS condensates floating in the sample. Each
1399 frame corresponds to a step of 0.125 μm, starting from a point 1.75 μm above the glass
1400 surface (z = 0 nm). Sample was prepared with glycogen (10g/L) in IS buffer mixed with
1401 GFP (15 μM) and 100 kDa PEG (200 μM) and imaging was performed at 30°C.

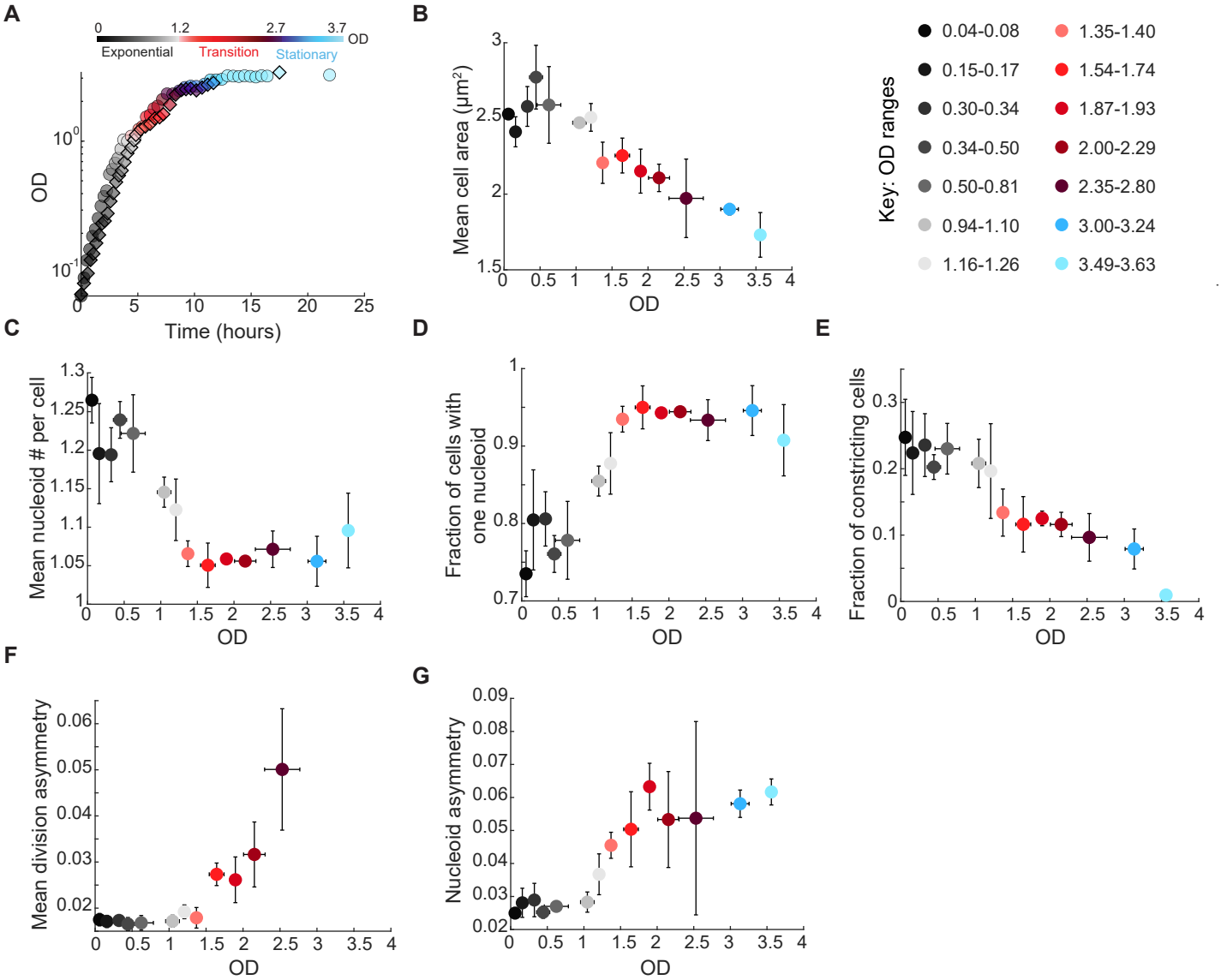
A
0
1.2
2.7
3.7
OD
Exponential
Transition
Stationary
OD
Time (hours)
B
Mean cell area (μm²)
OD
Key: OD ranges
0.04-0.08
0.15-0.17
0.30-0.34
0.34-0.50
0.50-0.81
0.94-1.10
1.16-1.26
1.35-1.40
1.54-1.74
1.87-1.93
2.00-2.29
2.35-2.80
3.00-3.24
3.49-3.63
C
Mean nucleoid # per cell
OD
D
Fraction of cells with one nucleoid
OD
E
Fraction of constricting cells
OD
F
Mean division asymmetry
OD
G
Nucleoid asymmetry
OD

Fig 1

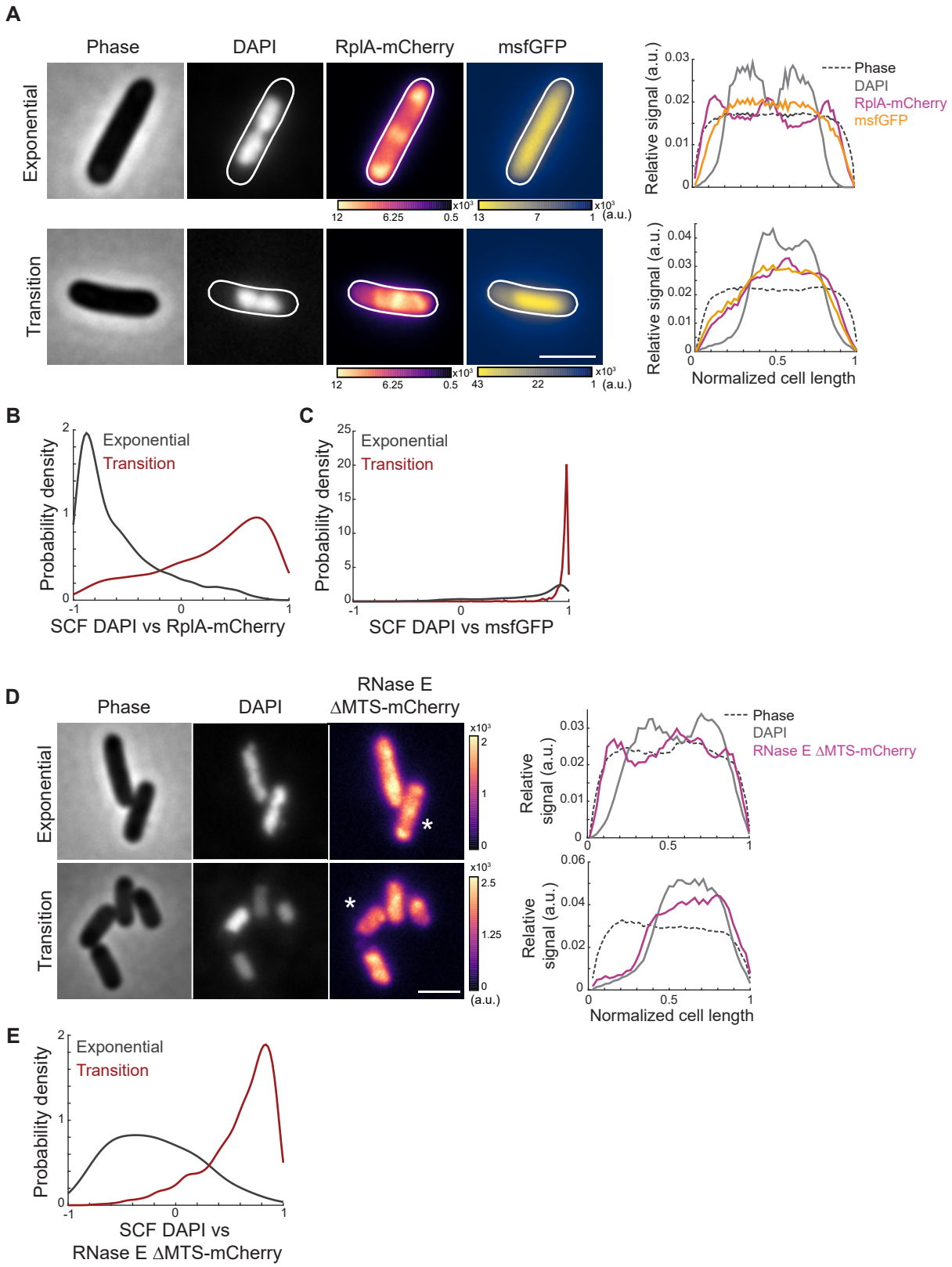
A
Phase
DAPI
RplA-mCherry
msfGFP
Exponential
Transition
Relative signal (a.u.)
Phase
DAPI
RplA-mCherry
msfGFP
Normalized cell length
B
Probability density
Exponential
Transition
SCF DAPI vs RplA-mCherry
C
Probability density
Exponential
Transition
SCF DAPI vs msfGFP
D
Phase
DAPI
RNase E
ΔMTS-mCherry
Exponential
Transition
Relative signal (a.u.)
Phase
DAPI
RNase E ΔMTS-mCherry
Normalized cell length
E
Probability density
Exponential
Transition
SCF DAPI vs
RNase E ΔMTS-mCherry

Fig 2

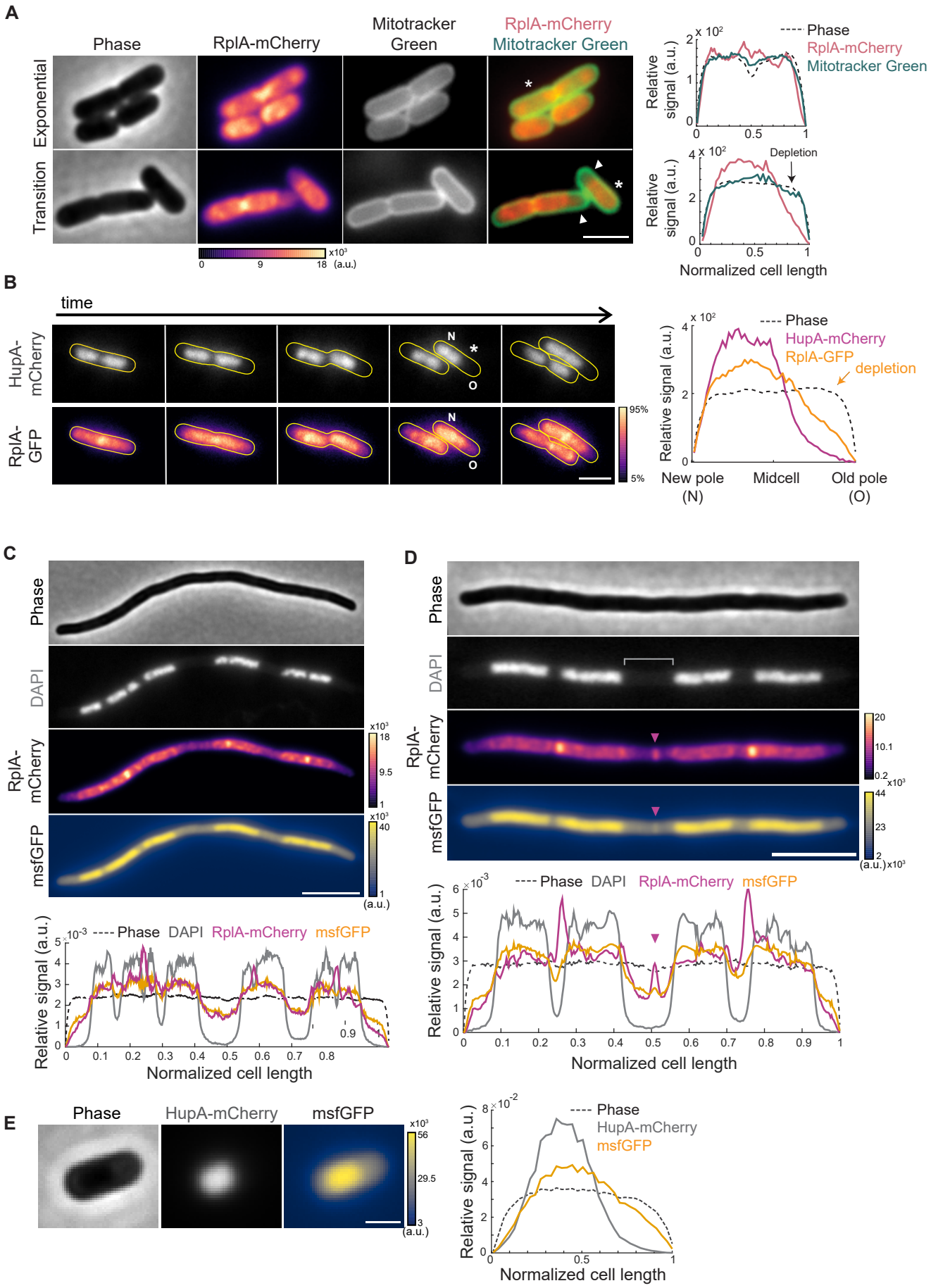
A
Phase
RplA-mCherry
Mitotracker Green
RplA-mCherry
Mitotracker Green
Exponential
Transition
x10³
0
9
18
(a.u.)
Phase
RplA-mCherry
Mitotracker Green
Relative signal (a.u.)
Depletion
Normalized cell length
B
time
HupA-mCherry
RplA-GFP
N
O
95%
5%
Phase
HupA-mCherry
RplA-GFP
depletion
Relative signal (a.u.)
New pole (N)
Midcell
Old pole (O)
C
Phase
DAPI
RplA-mCherry
msfGFP
(a.u.)
Phase DAPI RplA-mCherry msfGFP
Relative signal (a.u.)
Normalized cell length
D
Phase
DAPI
RplA-mCherry
msfGFP
(a.u.)
Phase DAPI RplA-mCherry msfGFP
Relative signal (a.u.)
Normalized cell length
E
Phase
HupA-mCherry
msfGFP
(a.u.)
Phase
HupA-mCherry
msfGFP
Relative signal (a.u.)
Normalized cell length

Fig 3

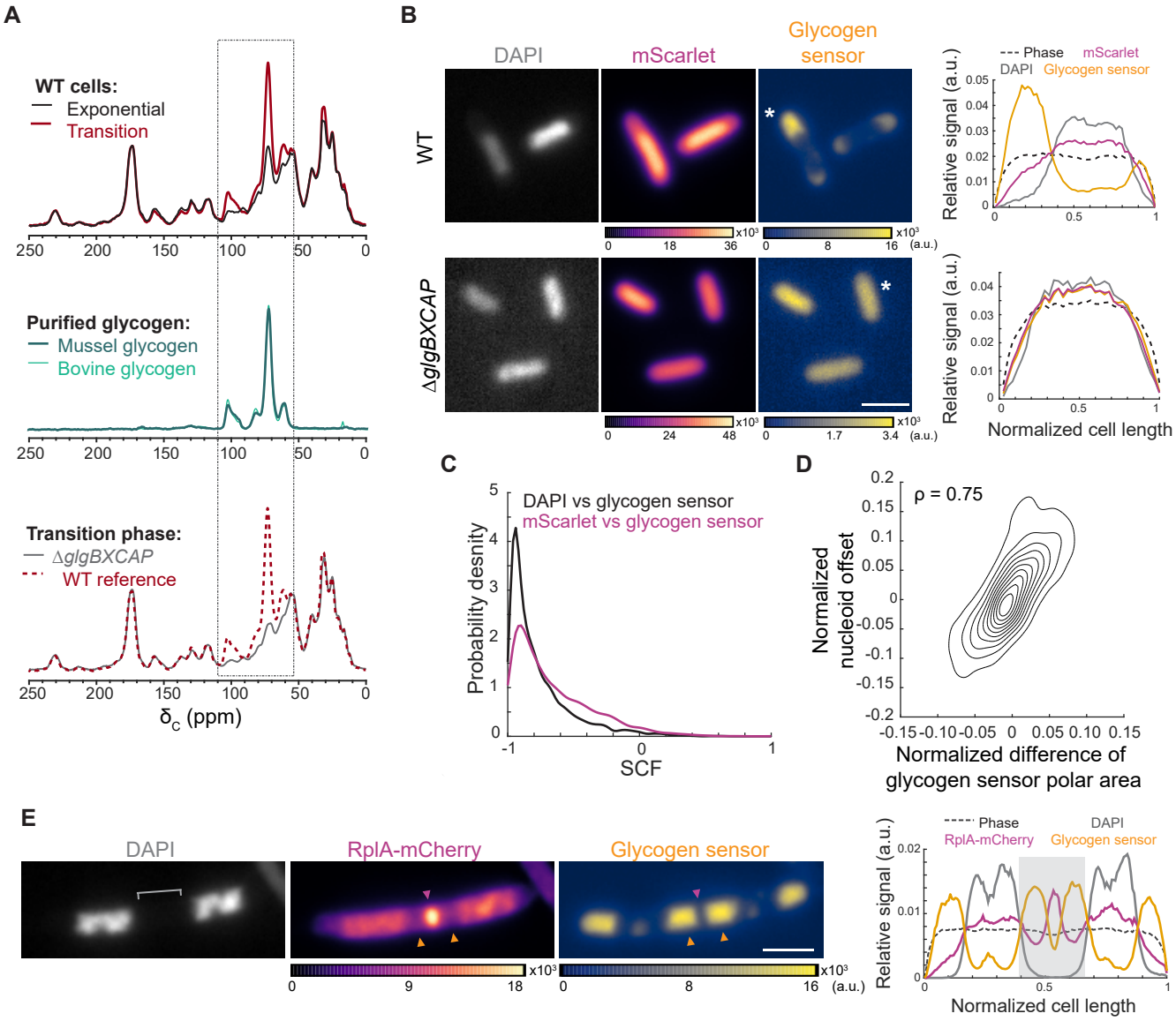
A
WT cells:
Exponential
Transition
Purified glycogen:
Mussel glycogen
Bovine glycogen
Transition phase:
ΔglgBXCAP
WT reference
δC (ppm)
B
DAPI
mScarlet
Glycogen sensor
WT
ΔglgBXCAP
Phase
mScarlet
DAPI
Glycogen sensor
Relative signal (a.u.)
Normalized cell length
C
DAPI vs glycogen sensor
mScarlet vs glycogen sensor
Probability desnity
SCF
D
ρ = 0.75
Normalized nucleoid offset
Normalized difference of glycogen sensor polar area

E
DAPI
RplA-mCherry
Glycogen sensor
Phase
RplA-mCherry
DAPI
Glycogen sensor
Relative signal (a.u.)
Normalized cell length

Fig 4

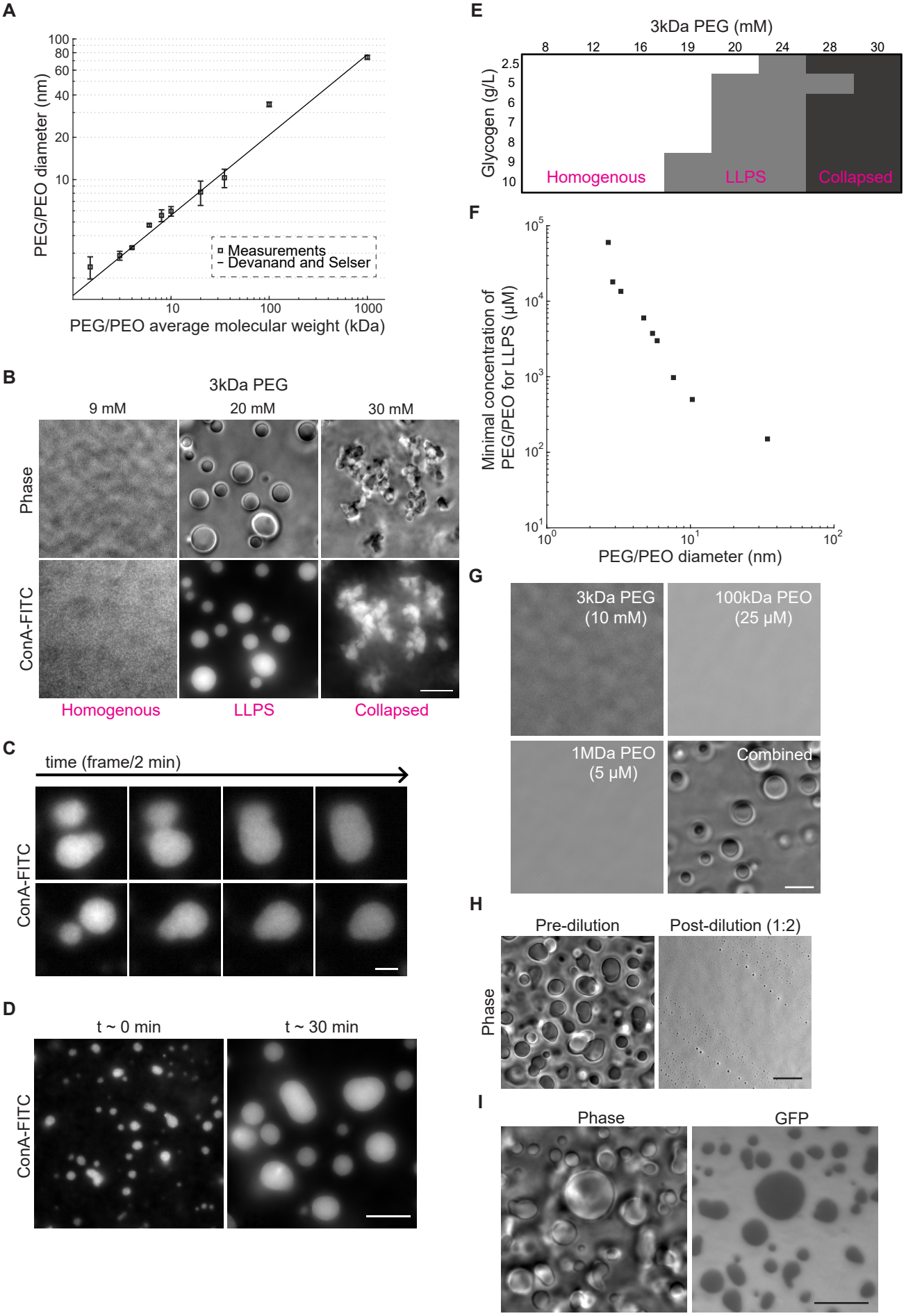
A
PEG/PEO diameter (nm)
PEG/PEO average molecular weight (kDa)
Measurements
Devanand and Selser
B
3kDa PEG
9 mM
20 mM
30 mM
Phase
ConA-FITC
Homogenous
LLPS
Collapsed
C
time (frame/2 min)
ConA-FITC
D
t ~ 0 min
t ~ 30 min
ConA-FITC
E
3kDa PEG (mM)
Glycogen (g/L)
Homogenous
LLPS
Collapsed
F
Minimal concentration of PEG/PEO for LLPS (μM)
PEG/PEO diameter (nm)
G
3kDa PEG (10 mM)
100kDa PEO (25 μM)
1MDa PEO (5 μM)
Combined
H
Pre-dilution
Post-dilution (1:2)
Phase
I
Phase
GFP

Fig 5

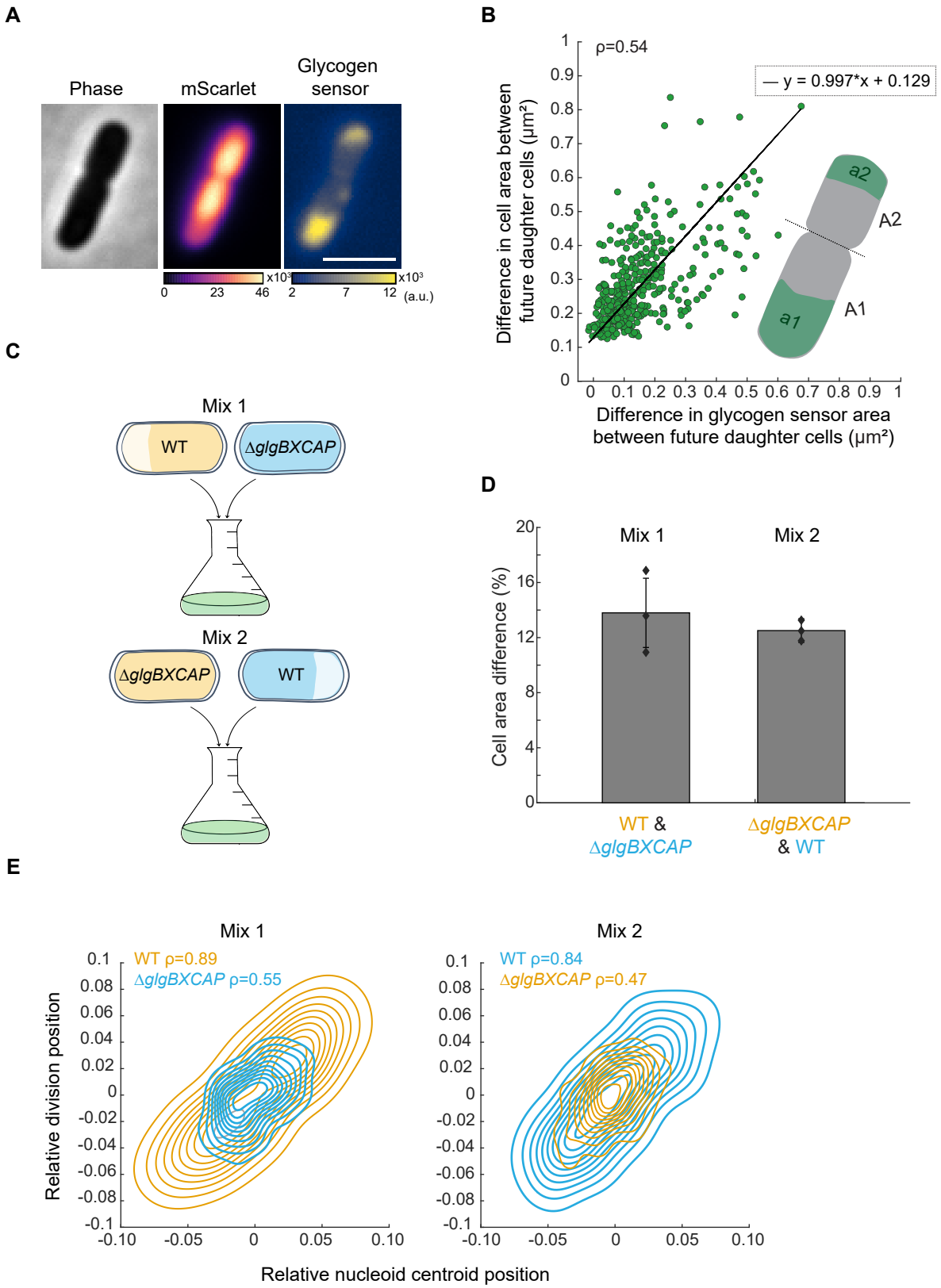
A
Phase
mScarlet
Glycogen sensor
0
23
46
x10³
2
7
12
x10³
(a.u.)
B
ρ=0.54
— y = 0.997*x + 0.129
Difference in cell area between future daughter cells (µm²)
Difference in glycogen sensor area between future daughter cells (µm²)
a2
A2
a1
A1
C
Mix 1
WT
ΔglgBXCAP
Mix 2
ΔglgBXCAP
WT
D
Mix 1
Mix 2
Cell area difference (%)
WT & ΔglgBXCAP
ΔglgBXCAP & WT
E
Mix 1
WT ρ=0.89
ΔglgBXCAP ρ=0.55
Mix 2
WT ρ=0.84
ΔglgBXCAP ρ=0.47
Relative division position
Relative nucleoid centroid position

Fig 6

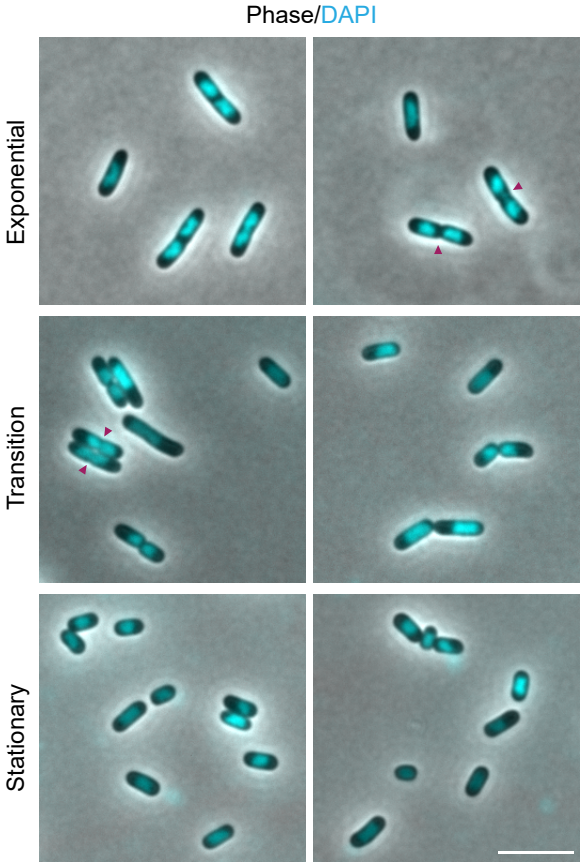

Fig EV1

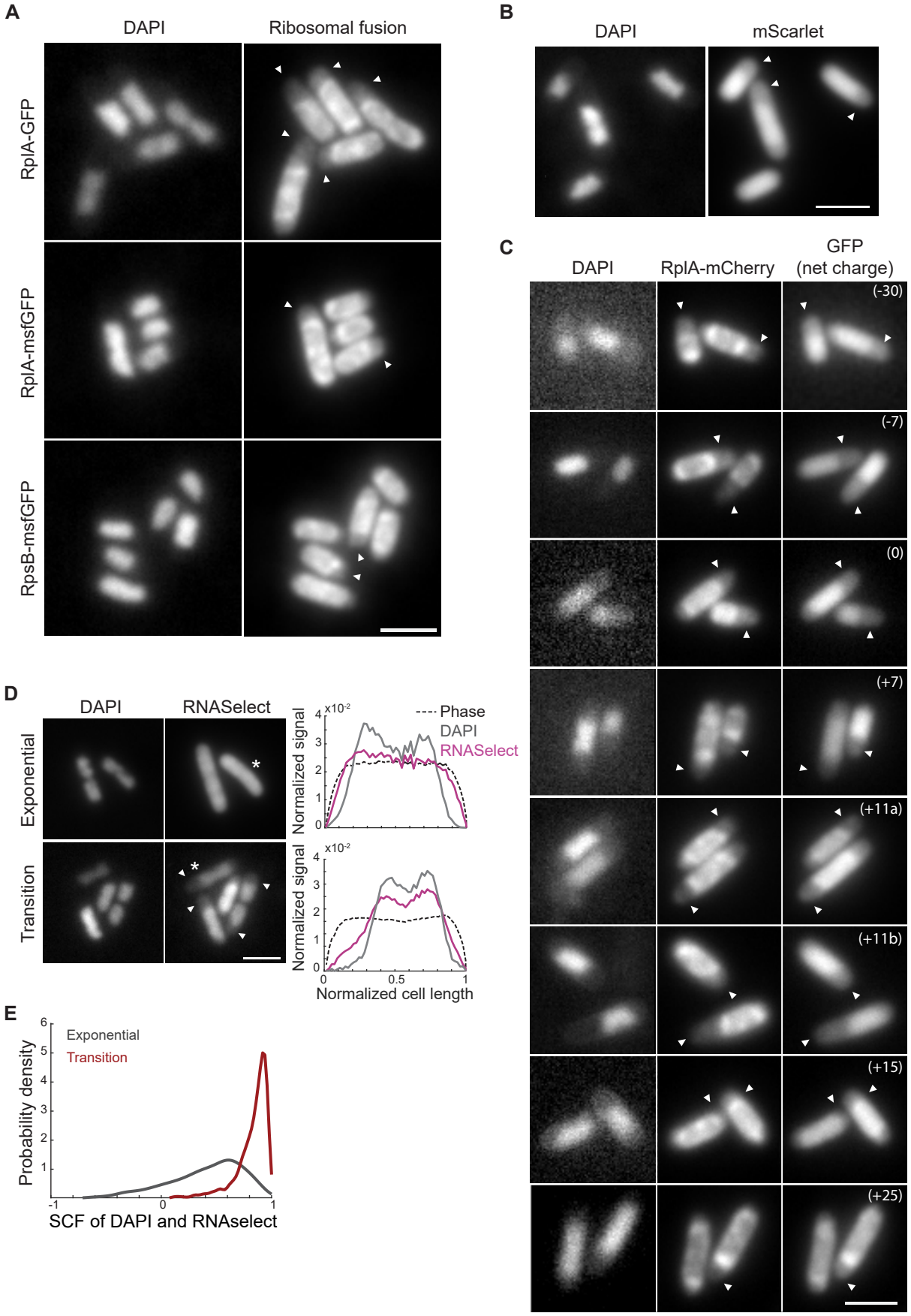
A
DAPI
Ribosomal fusion
RplA-GFP
RplA-msfGFP
RpsB-msfGFP
B
DAPI
mScarlet
C
DAPI
RplA-mCherry
GFP
(net charge)
(-30)
(-7)
(0)
(+7)
(+11a)
(+11b)
(+15)
(+25)
D
DAPI
RNASelect
Exponential
Transition
Phase
DAPI
RNASelect
Normalized signal
x10-2
Normalized cell length
E
Exponential
Transition
Probability density
SCF of DAPI and RNAselect

Fig EV2

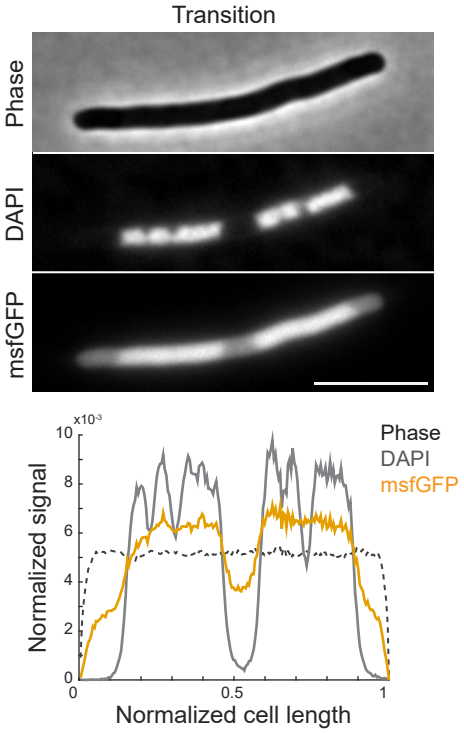
Transition
Phase
DAPI
msfGFP
x10-3
10
8
6
4
2
0
Normalized signal
0
0.5
1
Normalized cell length
Phase
DAPI
msfGFP

Fig EV3

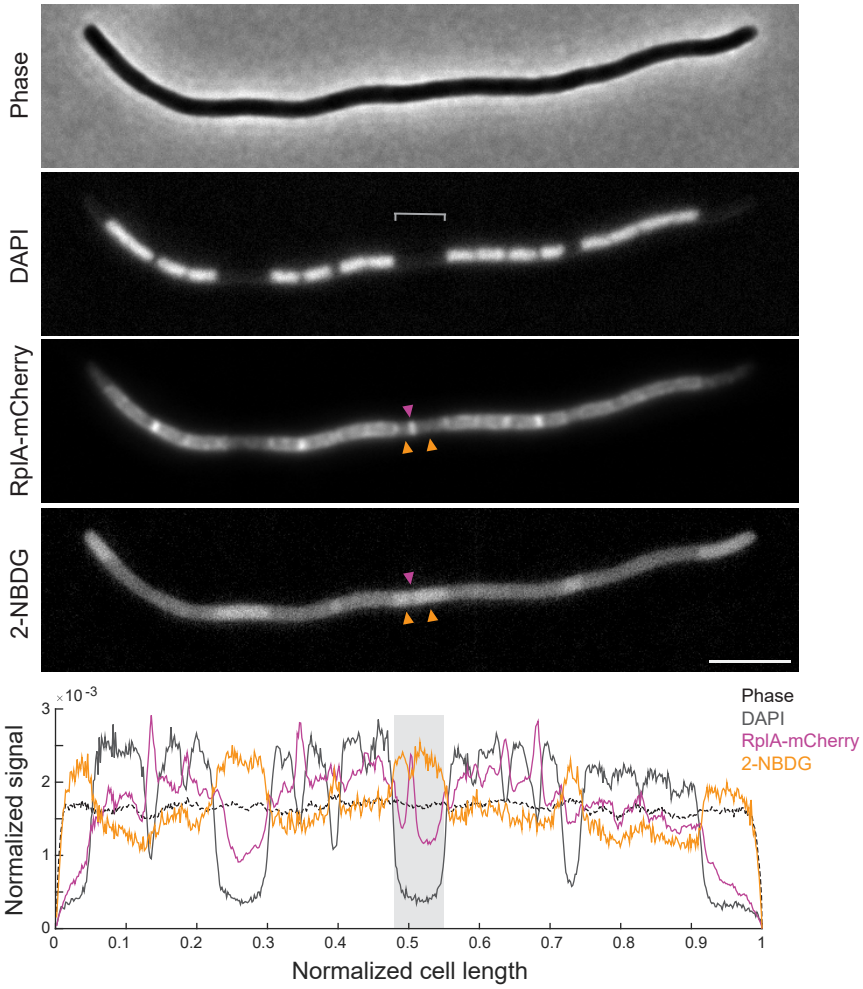
Phase
DAPI
RplA-mCherry
2-NBDG
Normalized signal
×10 -3
3
2
1
0
0
0.1
0.2
0.3
0.4
0.5
0.6
0.7
0.8
0.9
1
Normalized cell length
Phase
DAPI
RplA-mCherry
2-NBDG

Fig EV4

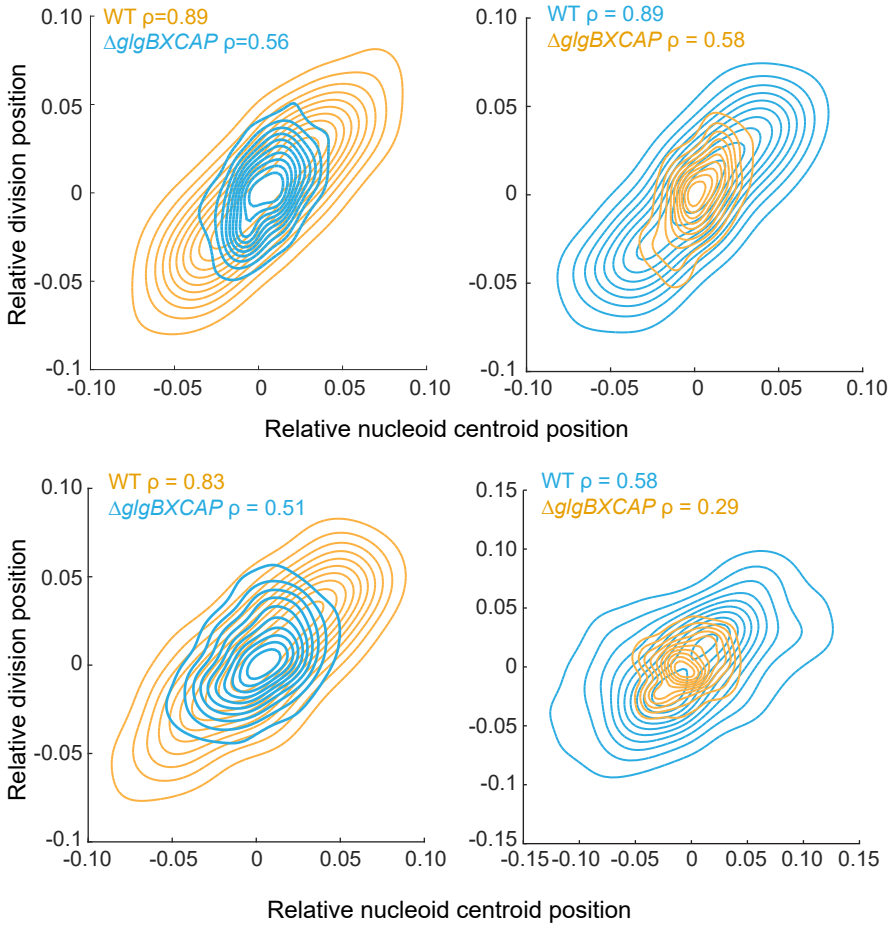
WT ρ=0.89
ΔglgBXCAP ρ=0.56
WT ρ = 0.89
ΔglgBXCAP ρ = 0.58
WT ρ = 0.83
ΔglgBXCAP ρ = 0.51
WT ρ = 0.58
ΔglgBXCAP ρ = 0.29
Relative division position
Relative nucleoid centroid position

Fig EV5